

Programmable Hierarchical Kirigami

Ning An, August G. Domel, Jinxiong Zhou, Ahmad Rafsanjani,* and Katia Bertoldi*

Kirigami—the Japanese art of cutting paper—has recently inspired the design of highly stretchable and morphable mechanical metamaterials that can be easily realized by embedding an array of cuts into a sheet. This study focuses on thin plastic sheets perforated with a hierarchical pattern of cuts arranged to form an array of hinged squares. It is shown that by tuning the geometric parameters of this hierarchy as well as thickness and material response of the sheets not only a variety of different buckling-induced 3D deformation patterns can be triggered, but also the stress–strain response of the surface can be effectively programmed. Finally, it is shown that when multiple hierarchical patterns are brought together to create one combined heterogeneous surface, the mechanical response can be further tuned and information can be encrypted into and read out via the applied mechanical deformation.

cut when flat and then exploit local elastic instabilities to transform into complex 3D configurations upon stretching.^[16–19] Interestingly, it has also been shown that the introduction of hierarchy into kirigami structures further enrich their functionality as it enables higher stretchability,^[20,21] wider tunability of the bandgaps,^[21–23] and larger negative Poisson's ratios.^[24,25] However, most of the previous studies on hierarchical kirigami metamaterials have considered thick sheets and focused on their in-plane deformation.^[20–25] The out-of-plane buckling behavior of thin hierarchical kirigami sheets remains largely unexplored, and the only closely related study focuses on a system in which patterned notches are introduced in addition to cuts to guide the pop-up in a preferred direction.^[11]

1. Introduction

The ability to program the mechanical response of materials and structures is enabling a wide set of innovative applications ranging from stretchable electronics and wearable devices^[1,2] to soft robots^[3–7] and drug delivery systems.^[8,9] Recently, kirigami—the Japanese art of paper cutting—has been identified as a powerful tool to realize programmable mechanical metamaterials.^[10–15] A key feature of kirigami metamaterials is that they are conveniently

Here, we demonstrate how structural hierarchy can be exploited to realize thin kirigami metamaterials with highly nonlinear mechanical responses and complex deformation-induced 3D pattern transformations. We first use a combination of experiments and numerical simulations to study the response under uniaxial tension of kirigami sheets with hierarchical cuts arranged to form an array of squares connected at their vertices via thin ligaments and investigate in detail both the effect of geometry as well as plasticity of the sheets. We find that for sufficiently small thicknesses, the behavior is completely different from that previously reported for thick sheets,^[20–30] as mechanical instabilities triggered by the applied deformation result in the formation of complex 3D patterns and sequential pop-up processes. We then show that the geometric parameters of the embedded hierarchy enable us to tune both the morphology of the buckling-induced 3D patterns as well as the stress–strain response of the surfaces. Finally, we demonstrate that by creating heterogeneous hierarchical kirigami surfaces, we can expand the range of attainable mechanical responses and encrypt information that can then be read out upon stretching.


N. An, Dr. A. G. Domel, Dr. A. Rafsanjani, Prof. K. Bertoldi
Harvard John A. Paulson School of Engineering and Applied Sciences
Harvard University
Cambridge, MA 02138, USA
E-mail: bertoldi@seas.harvard.edu

N. An, Prof. J. Zhou
State Key Laboratory for Strength and Vibration of Mechanical Structures
and School of Aerospace
Xi'an Jiaotong University
Xi'an 710049, P. R. China

Dr. A. Rafsanjani
Department of Materials
ETH Zürich
8093 Zürich, Switzerland
E-mail: ahmad.rafsanjani@mat.ethz.ch

Prof. K. Bertoldi
Kavli Institute
Harvard University
Cambridge, MA 02138, USA

Prof. K. Bertoldi
Wyss Institute for Biologically Inspired Engineering
Harvard University
Cambridge, MA 02138, USA

 The ORCID identification number(s) for the author(s) of this article can be found under <https://doi.org/10.1002/adfm.201906711>.

DOI: 10.1002/adfm.201906711

2. Hierarchical Kirigami Sheets

We consider a thin flat sheet (of thickness t) with a hierarchical cut pattern that produces square domains (see **Figure 1**). Hierarchical levels are defined as follows. At level 1, we introduce a square array of mutually orthogonal line cuts to create square domains of edge length l (with $t/l \ll 1$) separated by hinges of width δ_1 (see **Figure 1a**). At level 2, we construct the hierarchical pattern by further placing orthogonal line cuts into each of the square domains of the level 1 cuts to divide them into

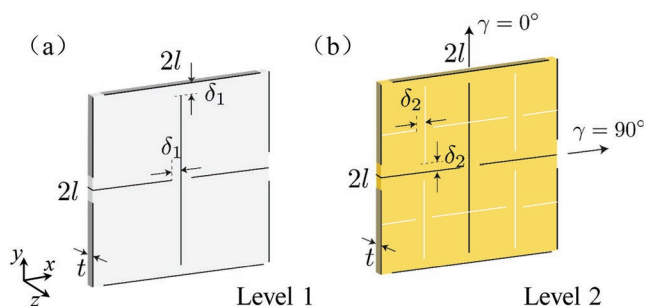


Figure 1. Schematics of the hierarchical kirigami structures with square pattern. a) Level 1 and b) level 2 and definition of $\gamma = 0^\circ$ and $\gamma = 90^\circ$ directions.

four squares of edge $l/2$ connected by hinges of width δ_1 and δ_2 (see Figure 1b). We study the mechanical response of this hierarchical system when uniaxially stretched along the edges of the squares. Since the level 1 and level 2 structures have fourfold and twofold symmetry, respectively, we load the former only in one direction, whereas for the latter we investigate the response for both $\gamma = 0^\circ$ and 90° (see Figure 1b).

3. Mechanical Response of Hierarchical Kirigami Sheets

3.1. Experiments

The response of our hierarchical kirigami structures are characterized using a uniaxial testing machine (Instron 5969) equipped with a 500 N load cell, while their out-of-plane deformation is monitored using a digital camera (Sony RX100V) placed in front of them. All samples are fabricated out of polyester plastic sheets (McMaster-Carr, product id: 9513K147) with thickness $t = 101.6 \mu\text{m}$, whose material properties are characterized via a uniaxial tensile test (see Figure S1 and Table S1 in the Supporting Information). Kirigami structures with $l = 8 \text{ mm}$ are manufactured out of these plastic sheets using a commercial laser cutter (Universal Laser Systems, Scottsdale, AZ), which produces slits with width of about 0.25 mm (see Section S1 in the Supporting Information).

In Figure 2, we report results for samples comprising 2×6 unit cells. We start by focusing on level 1 kirigami sheets characterized by $\delta_1/l = 0.0525$ and 0.15 (see Figure 2a). As previously observed,^[16] the stress–strain response of these kirigami sheets

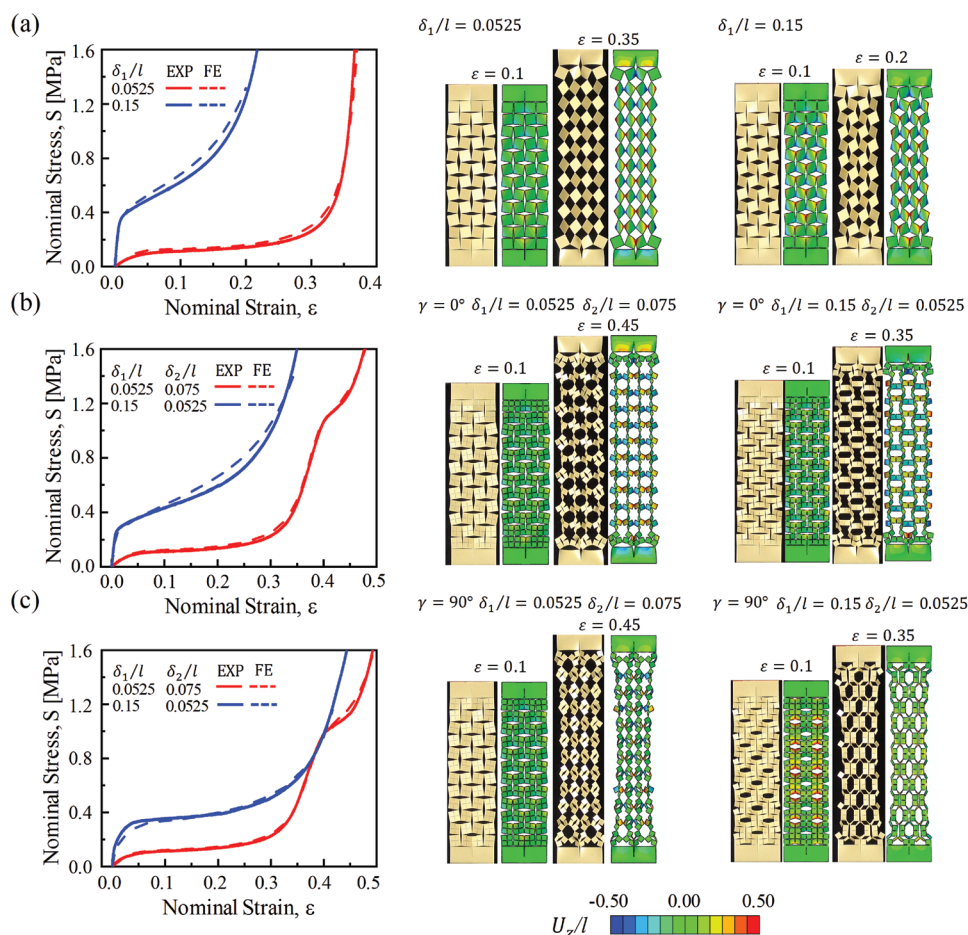


Figure 2. Mechanical response of hierarchical kirigami sheets subjected to uniaxial tension. Comparison between experimental and numerical stress–strain curves (left) and deformation at two different levels of applied strain ϵ (right) for a) level 1 structures; b) level 2 structures with $\gamma = 0^\circ$; c) level 2 structures with $\gamma = 90^\circ$. For the numerical images, we also show the distribution of the normalized out-of-plane displacement (U_z) in the deformed configurations.

is characterized by three distinct regions: i) an initial linear elastic response during which the samples deform in-plane; ii) a sudden departure from linearity to a plateau stress caused by out-of-plane buckling of the hinges and resulting in the formation of a 3D cubic pattern; iii) final stiffening when the deformation mechanism of the hinges switches from bending to stretching. Next, in Figure 2b,c, we focus on level 2 hierarchical kirigami sheets characterized by two different sets of hinge width $(\delta_1/l, \delta_2/l) = (0.0525, 0.075)$ and $(0.15, 0.0525)$ and investigate their response for both $\gamma = 0^\circ$ and $\gamma = 90^\circ$. We find that the hierarchical pattern significantly alters the mechanical response of the sheets and that the ratio δ_1/δ_2 plays a crucial role (see Movie S1 in the Supporting Information). More specifically, for $\delta_1/\delta_2 > 1$, the stress–strain response of the level 2 samples is similar to that of the level 1 system and characterized by an initial linear regime, a stress plateau, and final stiffening (see blue curves in Figure 2b,c). However, the buckling-induced 3D patterns are remarkably different from those observed for the level 1 samples and are affected by the loading direction. Differently, for the level 2 sheets with $\delta_1/\delta_2 < 1$, an unusual double-plateau stress–strain curve emerges (see red curves in Figure 2b,c), accompanied by a sequential pop-up process. First, the smaller hinges of width δ_1 buckle out-of-plane and leads to a 3D pattern similar to that observed for the level 1 sheets. Then, the bigger hinges of width δ_2 buckle and induce the formation of a different and more complex 3D pattern.

3.2. Numerical Analysis

To better understand the parameters controlling the interesting and rich behaviors observed in our experiments, we conduct finite element (FE) simulations using the commercial package Abaqus/Standard 2017. In all of our simulations, the models are discretized using 4-node rectangular shell elements with reduced integration (Abaqus element type S4R), and the cuts in the sheets are modeled as thin rectangular slits with a thickness of 0.25 mm (as observed in the physical samples). The material behavior of the sheets is captured using an elastoplastic model with parameters directly extracted from uniaxial tensile tests conducted on the polyester plastic sheets (i.e., Young's modulus $E = 5.17$ GPa, Poisson's ratio $\nu = 0.4$, and yield stress $\sigma_y = 51.7$ MPa—see Figure S1 and Table S1 in the Supporting Information). Moreover, to understand the effect of plastic deformation, we also compare our results to those obtained by using a purely elastic material model with $E = 5.17$ GPa and $\nu = 0.4$.

We start by performing full finite size simulations on structures made out of an elastoplastic material that comprise an array of 2×6 cells (identical to the samples used in experiments). For these analyses, the lower boundary of the sample is fixed and a vertical displacement is applied to the upper boundary, while the lateral boundaries are assumed to be traction free. The response of the sheets is simulated by conducting dynamic implicit simulations (*DYNAMIC module in Abaqus) and quasi-static conditions are ensured by monitoring the kinetic energy. Finally, to trigger the instability, an imperfection is introduced by applying two opposing small bias forces normal to the sheet plane at the longer side of each cut during the initial step of each simulation. As shown

in Figure 2, we find excellent agreement between the numerical and experimental results, confirming the validity of these numerical analyses.

Having validated our FE analyses, we next use them to understand the role played both by material properties and thickness of the sheets. Toward this end, we simulate the response of the two hierarchical patterns considered in Figure 2 (which are characterized by $(\delta_1/l, \delta_2/l) = (0.0525, 0.075)$ and $(0.15, 0.0525)$) embedded into sheets of different thickness, whose material response is captured using both elastoplastic and purely elastic constitutive models. To reduce the computational cost and ensure the response is not affected by boundary effects, in all these analyses, we consider infinite periodic structures using representative unit cells with suitable periodic boundary conditions (see Figure S4 in the Supporting Information for comparison between finite size and unit cell simulations). The simulations consist of two steps: i) we first use a linear perturbation analysis (*BUCKLING module in Abaqus) to identify the critical buckling mode; ii) we then introduce a small imperfection in the form of the critical mode into the mesh to trigger the instability and conduct dynamic implicit simulations to investigate the response under the applied loading.

First, we examine the effect of plasticity and investigate the response of both elastic and elastoplastic kirigami sheets with thickness $t/l = 0.0127$ (as in our experiments shown in Figure 2). The results reported in Figure 3a (for $\gamma = 0^\circ$) and Figure 3b (for $\gamma = 90^\circ$) indicate that plastic deformation significantly affects the stress–strain response of the structures past the initial linear regime. For a purely elastic hierarchical kirigami sheet, the plateau caused by the out-of-plane buckling of the hinges is not as accentuated as in the presence of plasticity. Moreover, in the case of a purely elastic material the second plateau observed in both experiments and elastoplastic simulations is suppressed for the structure with $\delta_1/\delta_2 < 1$, as the response is dominated by the stretching of the δ_1 ligaments. As such, these results suggest that analyses based on a linear material response^[11,13,14,31] may not fully capture the response of kirigami sheets, since the large local strains are expected to induce plastic deformation in most materials. However, it is important to note that plastic deformation does not affect the

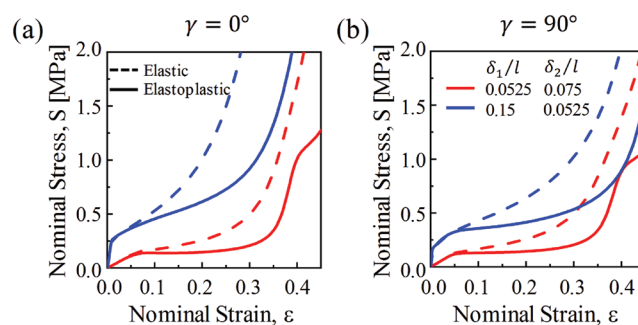


Figure 3. Effect of material behavior on the response of hierarchical kirigami sheets subjected to uniaxial tension. Comparison between numerical stress–strain curves obtained considering an elastoplastic (solid line) and a purely elastic (dashed line) material model. Results for two different hierarchical patterns are reported, characterized by $(\delta_1/l, \delta_2/l) = (0.0525, 0.075)$ (in red) and $(0.15, 0.0525)$ (in blue), for both a) $\gamma = 0^\circ$ and b) $\gamma = 90^\circ$.

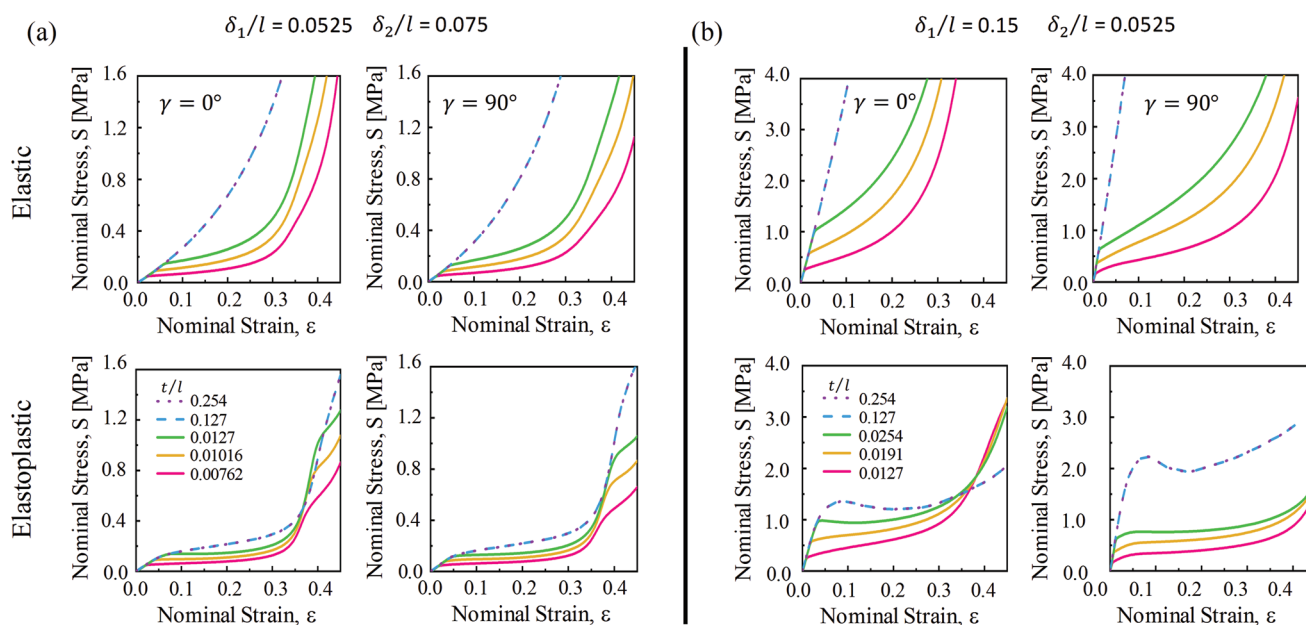


Figure 4. Effect of thickness on the response of hierarchical kirigami sheets subjected to uniaxial tension. Stress–strain curves obtained for a purely elastic (top row) and elastoplastic (bottom row) material response. Two different patterns are considered characterized by a) $(\delta_1/l, \delta_2/l) = (0.0525, 0.075)$ and b) $(\delta_1/l, \delta_2/l) = (0.15, 0.0525)$. Stress–strain curves for both $\gamma = 0^\circ$ and $\gamma = 90^\circ$ are reported.

morphology of the emerging 3D patterns, as the characteristics of those are found to be unaltered (see Figure S11 in the Supporting Information).

Next, we investigate the effect of the sheet thickness and simulate the behavior of kirigami sheets with increasing values of t for both purely elastic and elastoplastic material response. The results reported in **Figure 4** show that the initial linear response is never affected by t . Differently, the critical strain ϵ_c at which the stress departs from linearity (because of out-of-plane buckling of the ligaments) is found to initially monotonically increase with t , $\epsilon_c \approx 0.5(t/\delta_1)^2$ (see Figure S12 in the Supporting Information). However, there is a critical thickness t_{cr} above which the thickness has no more effect on the mechanical response and all stress–strain curves collapse on top of each other. By inspecting the deformation modes (**Figure 5**), we find that t_{cr} marks the transition between out-of-plane and in-plane deformation. For $t < t_{cr}$ (i.e., for thin sheets), the system buckles out-of-plane, whereas for $t > t_{cr}$ (i.e., for thick sheets), it deforms in-plane. Note that thick elastoplastic kirigami sheets still exhibit a plateau in their stress–strain response. However, such plateau has different nature from that emerging in thin structures as it is associated with the yielding of the material due to stretching of the hinges and does not correspond to out-of-plane buckling.

By comparing the stress–strain curves of **Figure 4**, we also find that the response of the hierarchical kirigami sheet with $\delta_1/\delta_2 < 1$ is much more sensitive to the loading direction than that of the system with $\delta_1/\delta_2 > 1$. Such sensitivity is also reflected in the deformation modes reported in **Figure 5**. For the kirigami sheet with $\delta_1/\delta_2 < 1$, only the ligaments with width δ_1 initially deform (for thin sheets they buckle out-of-plane, while for thick sheets they bend in-plane), giving rise to a pattern similar to that of level 1 systems. As the applied strain increases, also the ligaments with width δ_2 deform and a second

distinct pattern emerges which is not significantly affected by the loading direction. Differently, for the level 2 system with $\delta_1/\delta_2 > 1$, all ligaments deform simultaneously from the very beginning, resulting in the formation of two distinct pattern for $\gamma = 0^\circ$ and $\gamma = 90^\circ$. For these structures, an increase in the applied strain does not lead to qualitative changes of the 3D pattern and only results in its accentuation.

4. Heterogeneous Hierarchical Kirigami Sheets

Having understood the effect of geometry and material behavior on the mechanical response of our hierarchical kirigami sheets, we next use FE analyses to fully explore the design space and simulate the response of thin elastoplastic sheets with $t/l = 0.0127$ and embedded hierarchical pattern characterized by $\delta_1/l \in [0.0525, 0.15]$ and $\delta_2/l \in [0.0525, 0.1]$ (see Figures S5–S7 in the Supporting Information). We then use this numerical database to further expand the design space by investigating the response of heterogeneous surfaces comprising kirigami patterns characterized by different geometric parameters.

4.1. Programming Stress–Strain Response

We begin by focusing on combined heterogeneous surfaces that comprise n hierarchical kirigami patterns connected in series (see **Figure 6a**) and develop a numerical algorithm that takes as input the stress–strain curves obtained via the unit cell simulations and combine them to predict the response of the system. Toward this end, we start by noting that the equilibrium states for such heterogeneous system are given by (see Section S3A in the Supporting Information)

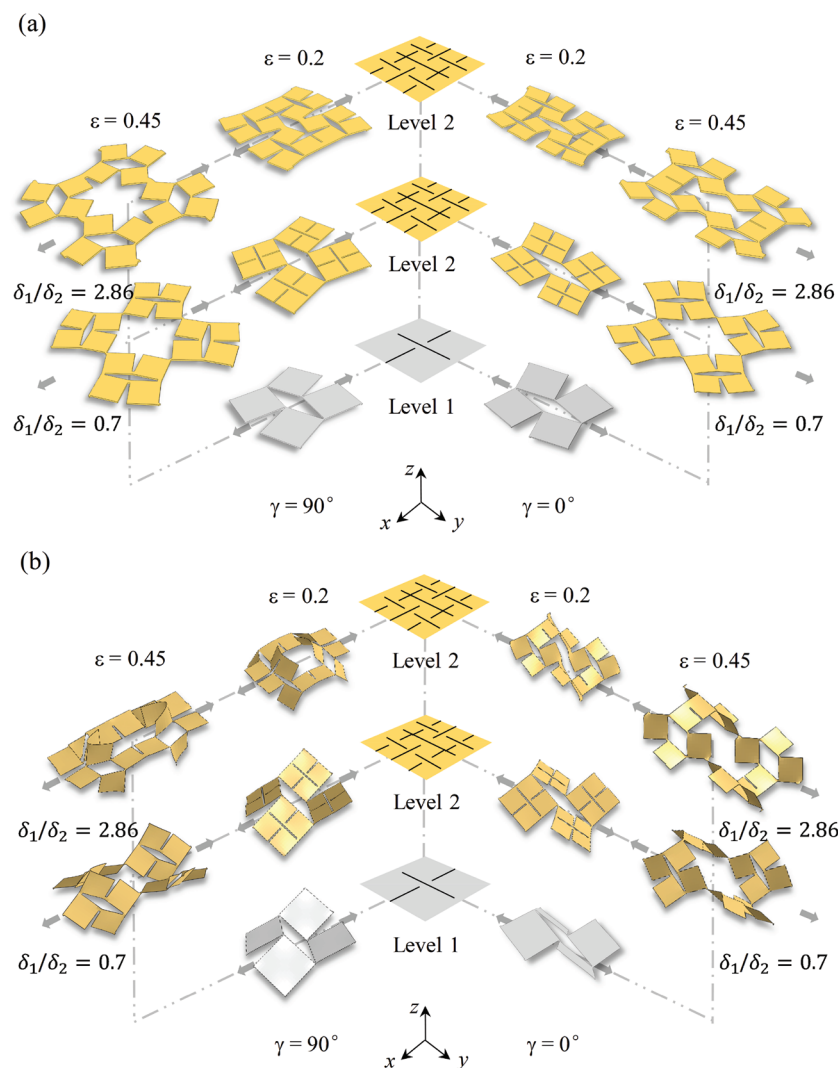


Figure 5. Numerical snapshots of kirigami sheets at different levels of applied deformation. We show a level 1 pattern characterized by $\delta_1/l = 0.0525$ (in gray) and level 2 patterns characterized by $(\delta_1/l, \delta_2/l) = (0.0525, 0.075)$ and $(\delta_1/l, \delta_2/l) = (0.15, 0.0525)$ (in yellow). Sheets with a) $t/l = 0.127$ deform in-plane, whereas sheets with b) $t/l = 0.0127$ deform out-of-plane.

$$S^{(i)}(\epsilon^{(i)}) - S^{(n)}(\epsilon^{(n)}) = 0, \quad \text{for } i = 1, \dots, n-1 \quad (1)$$

with

$$\epsilon L = \sum_{i=1}^n \epsilon^{(i)} L^{(i)} \quad (2)$$

where $S^{(i)}$, $\epsilon^{(i)}$, and $L^{(i)}$ denote the (nominal) stress, strain, and initial length of the i th building block (characterized by $\delta_1^{(i)}/l$ and $\delta_2^{(i)}/l$), respectively, $L = \sum_{i=1}^n L^{(i)}$, and ϵ is the applied strain. Therefore, to predict the response of a heterogeneous kirigami surface, we do not need to simulate the entire system, but we can simply use Equations (1) and (2) and the stress–strain curves obtained via our unit cell simulations (see Figures S5–S7 in the Supporting Information). Note that Equation (1) ensures that the nominal stress is the same in all n building blocks connected in series when the system is subjected to uniaxial

tension, while Equation (2) states that the total elongation of the sheet is given by the sum of the elongations of each building block.

In Figure 6, we consider a heterogeneous surface comprising two building blocks composed of 2×5 unit cells (so that $L^{(1)} = L^{(2)} = 10l$) characterized by $\delta_1^{(1)}/l = 0.0525$ (level 1) and $\delta_1^{(2)}/l = 0.15$, $\delta_2^{(2)}/l = 0.0525$, and $\gamma^{(2)} = 90^\circ$ (see Figure 6a,b). While both these two building blocks are characterized by a stress–strain curve with a single plateau, it is interesting to note that our model can predict that two stress plateaus emerge when they are combined (see Figure 6c,d and Movie S3 in the Supporting Information). The sequential buckling behavior of the heterogeneous surface is also apparent in Figure 6e, where we report the evolution of $\epsilon^{(1)}$ and $\epsilon^{(2)}$ as a function of the applied strain ϵ . As ϵ increases, $\epsilon^{(1)}$ increases first, while $\epsilon^{(2)}$ eventually increases only after $\epsilon^{(1)}$ has plateaued. We also note that by altering the length ratio of the building blocks, $L^{(1)}/L^{(2)}$, we are able to further tune the critical strain where the stress plateau will occur as well as the length of the stress plateau (see Figure 6f and Movie S4 in the Supporting Information). To validate the predictions of our model, we also compare its results to those obtained via both FE simulations and experiments. The excellent quantitative agreement between the three sets of data indicate that our simple analytical model can be used to rapidly explore the design space and identify combinations leading to target responses. Particularly, in Figure 7, we report the analytical prediction for the response of different heterogeneous surfaces comprising $n = 2$ building blocks. One building block is fixed to be a level 1 system with $\delta_1^{(1)}/l = 0.0525$, while the other one is one of level 2 systems with $\delta_2^{(2)}/l = 0.1$ and $\delta_1^{(2)}/\delta_2^{(2)} \in [0.525, 1.5]$. It can be seen from

the plots that by creating the heterogeneous surfaces, we obtain much more tunability and programmability of the stress–strain responses.

4.2. Programming Surface Texture

While so far we have looked at different building blocks arranged in series, we now explore the possibility of arranging them in 2D space. We note that if we arrange arbitrary kirigami patterns in parallel, they strongly affect each other, so that the response of the heterogeneous system cannot be predicted only based on the behavior of the building blocks (see Section S3B in the Supporting Information). To overcome this issue, we combine two different patterns with similar stress–strain behavior but distinct deformation modes into regions of the 2D space to define a target image. This results

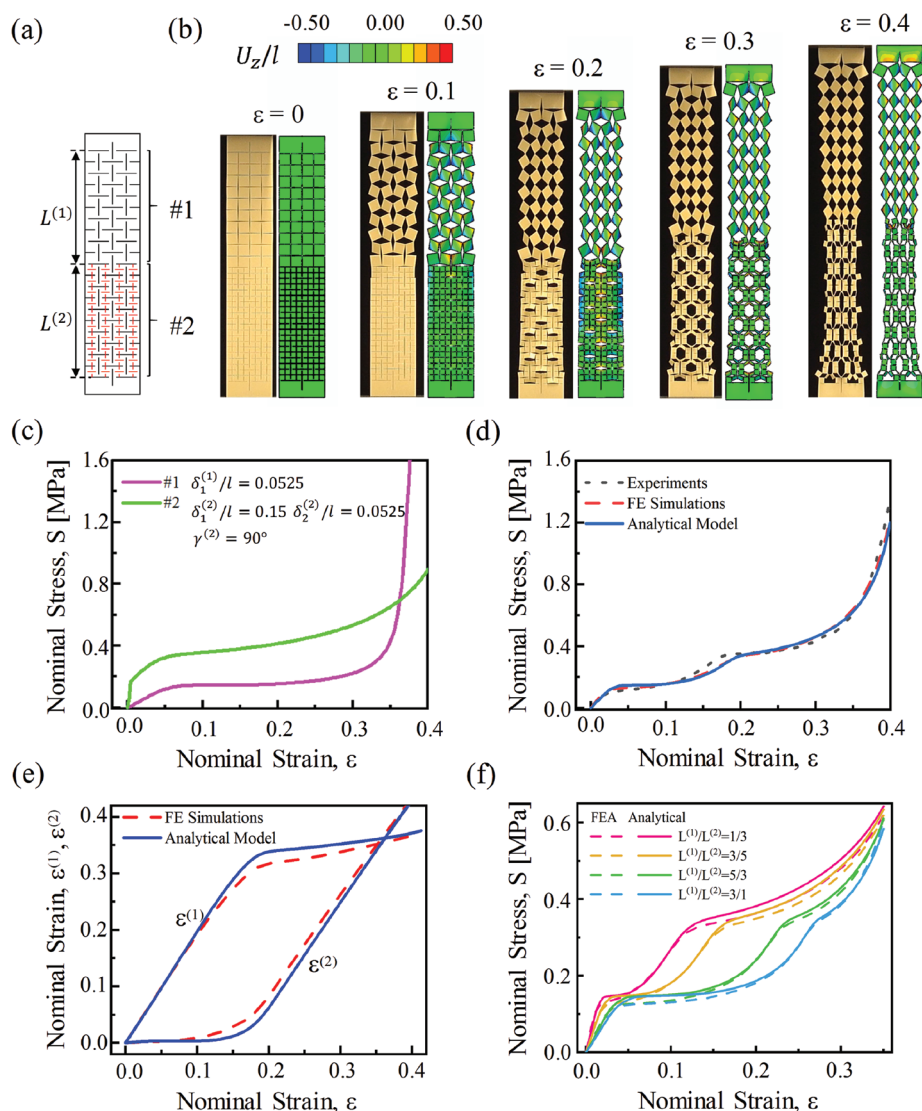


Figure 6. a) Schematic of our heterogeneous kirigami surface. b) Experimental and numerical snapshots of the heterogeneous kirigami surface at different levels of applied strain. For the numerical images, we also show the distribution of the normalized out-of-plane displacement (U_z) in the deformed configurations. c) Stress–strain response of the two individual building blocks. d) Stress–strain response of the combined heterogeneous surface as predicted by our analytical model (solid line) experiments (dotted line) and FE simulations (dashed line). e) Evolution of $\varepsilon^{(1)}$ and $\varepsilon^{(2)}$ as a function of the applied strain ε . f) Stress–strain response of the combined heterogeneous surface with building blocks characterized by different lengths.

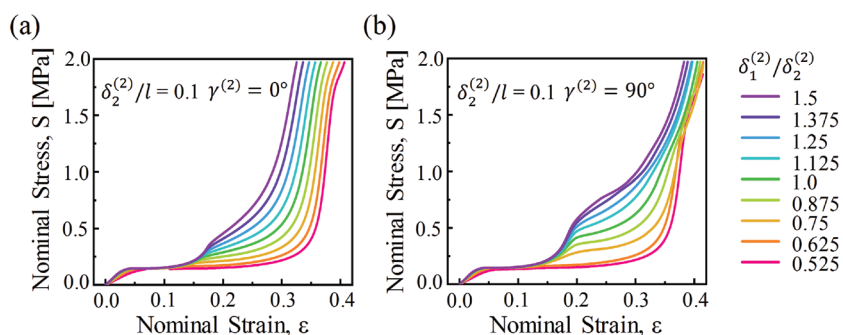


Figure 7. Mechanical response of heterogeneous surfaces comprising a level 1 system (with $\delta_1^{(1)}/l = 0.0525$) and a level 2 system with $\delta_2^{(2)}/l = 0.1$, $\delta_1^{(2)}/\delta_2^{(2)} \in [0.525, 1.5]$ and a) $\gamma^{(2)} = 0^\circ$ and b) $\gamma^{(2)} = 90^\circ$.

in heterogeneous surfaces with the same stress–strain response of the building blocks, but capable of revealing information (in form of an image) as soon as the system is subjected to uniaxial stretching to induce out-of-plane buckling.

Realization of such surfaces require knowledge not only of the stress–strain response of the building blocks, but also of their deformation modes. To this end, we quantify the difference in the emerging buckling-induced patterns by calculating the projected configurations (ϕ being defined as the ratio between the total hole area and the total area

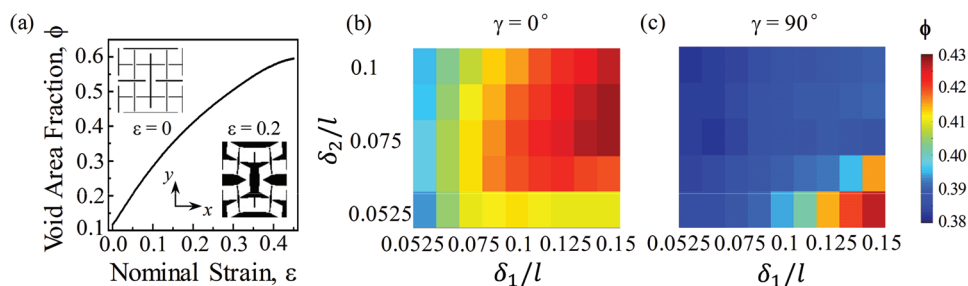


Figure 8. a) Evolution of void area fraction ϕ as a function of the applied strain ε for a level 2 pattern characterized by $\delta_1/l = 0.15$, $\delta_2/l = 0.0525$, and $\gamma = 0^\circ$. ϕ is calculated as the ratio between the hole area (black area in the snapshots) and the total area of the snapshots. b,c) Effect of δ_1/l and δ_2/l on the void area fraction ϕ at $\varepsilon = 0.2$ for level 2 patterns with b) $\gamma = 0^\circ$ and c) $\gamma = 90^\circ$.

as measured in pictures with front view). As shown in **Figure 8**, we find that for all kirigami sheets ϕ increases monotonically with the applied strain ε . Moreover, larger values of δ_1/l always

lead to a larger ϕ for both $\gamma = 0^\circ$ and $\gamma = 90^\circ$ loading. Differently, larger values of δ_2/l result in larger ϕ for $\gamma = 0^\circ$ loading and smaller ϕ for $\gamma = 90^\circ$ loading.

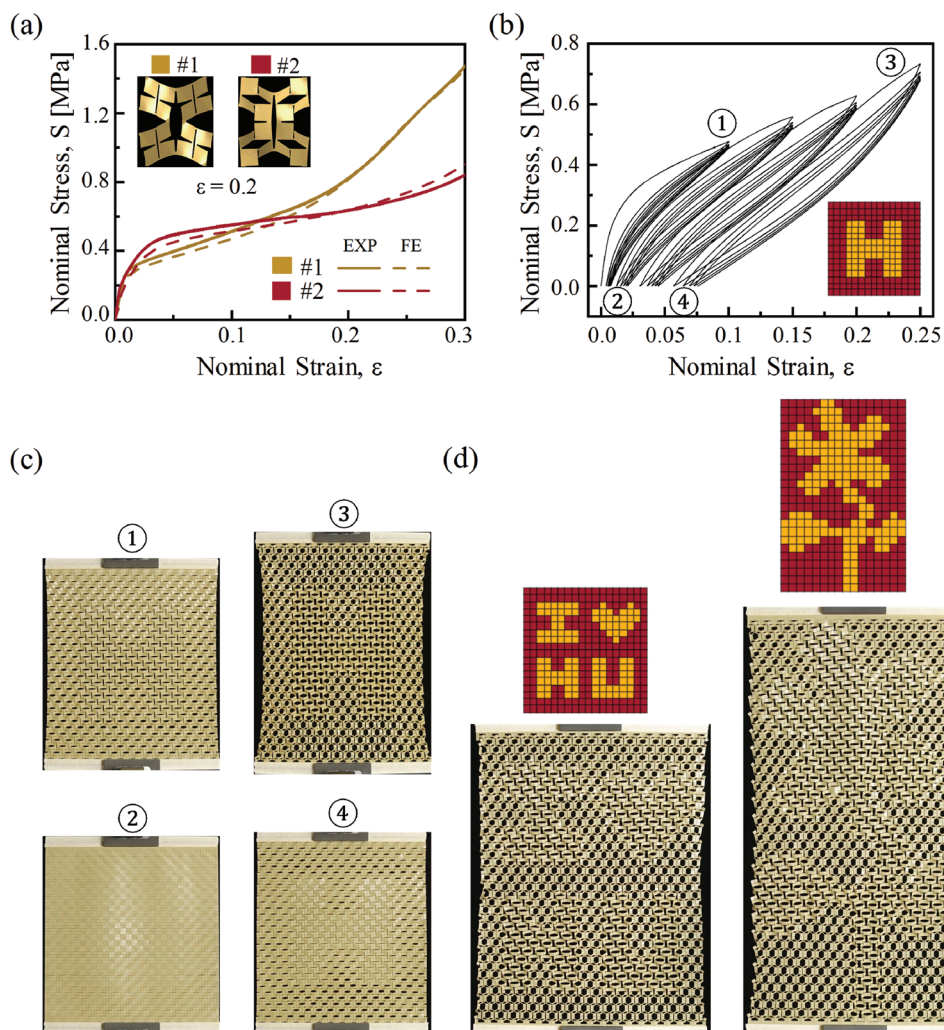


Figure 9. Design of a set of kirigami textured surfaces with embedded shapes with two unit cells as building blocks. a) Stress–strain response of the two unit cells with deformed patterns at a strain of 0.2. #1 is characterized by $\delta_1^{(1)}/l = 0.1375$, $\delta_2^{(1)}/l = 0.075$ and $\gamma^{(1)} = 0^\circ$, and #2 is characterized by $\delta_1^{(2)}/l = 0.15$, $\delta_2^{(2)}/l = 0.075$ and $\gamma^{(2)} = 90^\circ$. b) Stress–strain response of a kirigami textured surface with an embedded H recorded during a cyclic test, and c) experimental images captured right after the applied strain is increased to $\varepsilon = 0.1$ and 0.25 and then the load is dropped to zero. d) Design of kirigami textured surfaces with embedded “I ♥ HU” and a flower using patterns characterized by $\delta_1^{(1)}/l = 0.125$, $\delta_2^{(1)}/l = 0.0525$, $\gamma^{(1)} = 0^\circ$, and $\delta_1^{(2)}/l = 0.15$, $\delta_2^{(2)}/l = 0.0525$ and $\gamma^{(2)} = 90^\circ$.

By inspecting our numerical databases (Figures S5–S7, Supporting Information; Figure 8), we find multiple pairs of patterns with similar stress–strain responses, but different buckling-induced void area fractions ϕ . One of these is characterized by $\delta_1^{(1)}/l=0.1375$, $\delta_2^{(1)}/l=0.075$, $\gamma^{(1)}=0^\circ$ and $\delta_1^{(2)}/l=0.15$, $\delta_2^{(2)}/l=0.075$ and $\gamma^{(2)}=90^\circ$. As shown in Figure 9a, the mechanical response of these two patterns is very close, whereas their projected void area fraction at $\varepsilon=0.2$ are $\phi^{(1)}=0.43$ and $\phi^{(2)}=0.38$ (see Figure 8). To demonstrate the concept, we arrange the two patterns on a square domain and use the first to define the letter H and the second one to form the background (see Figure 9b). While the initially flat heterogeneous surface seems homogeneous (see panel 2 in Figure 9c at $\varepsilon \equiv 0$), the H shape emerges as soon as the system buckles out-of-plane at $\varepsilon \approx 0.1$. Interestingly, by performing cyclic tensile tests at different levels of applied tensile strain, we also find that the response of the system is largely reversible, suggesting potential use in optical displays and encryption. Note that the concept can be extended to different combinations of hierarchical patterns and an endless set of encrypted images. For example, in Figure 9d, we show that a variety of complex images can be encrypted in heterogeneous surfaces built using patterns characterized by $\delta_1^{(1)}/l=0.125$, $\delta_2^{(1)}/l=0.0525$, $\gamma^{(1)}=0^\circ$, and $\delta_1^{(2)}/l=0.15$, $\delta_2^{(2)}/l=0.0525$ and $\gamma^{(2)}=90^\circ$, for which $\phi^{(1)}=0.41$ and $\phi^{(2)}=0.43$ at $\varepsilon=0.2$ (see Figure 8). As such, our results indicate that in addition to notches,^[11] multistability,^[14] and aperiodicity,^[17] also hierarchical cuts can be exploited to realize displays and encryption based on kirigami principles.

5. Conclusion

In summary, we demonstrated that the introduction of hierarchical cuts into flat kirigami sheets further enriches the mechanical response of the system. More specifically, we found that by carefully choosing the thickness of the sheets and the width of the hinges associated with to each hierarchical level, the stress–strain response of the surface can be effectively programmed as well as a variety of different buckling-induced 3D deformation patterns can be triggered. Moreover, our results indicate that by combining different hierarchical patterns together, not only the range of achievable mechanical responses can be further expanded, but also information can be encrypted into the structure. As such, our work contributes to the field of programmable materials and morphological computations and opens avenues for the design of smart soft skins with multimodal functionalities. With such control of the mechanical response, we envision hierarchical kirigami surfaces could be integrated into soft robotic materials to create tactile sensors, smart displays, or friction-controlled skins that facilitate the interaction with the surrounding environment.

Supporting Information

Supporting Information is available from the Wiley Online Library or from the author.

Acknowledgements

N.A. and A.G.D. contributed equally to this work. N.A. acknowledges support from the China Scholarship Council (File No. 201706280229). N.A. and J.Z. acknowledge support from the National Natural Science Foundation of China Grants 11472210 and 11372239. A.R. acknowledges support from the Swiss National Science Foundation under grant P3P3P2-174326. K.B. acknowledges support from the NSF Grant DMR-1420570.

Conflict of Interest

The authors declare no conflict of interest.

Keywords

hierarchical cuts, kirigami, mechanical metamaterials, programmable response

Received: August 15, 2019

Revised: October 11, 2019

Published online:

- [1] Y. Su, X. Ping, K. J. Yu, J. W. Lee, J. A. Fan, B. Wang, M. Li, R. Li, D. V. Harburg, Y. Huang, C. Yu, S. Mao, J. Shim, Q. Yang, P.-Y. Lee, A. Armonas, K.-J. Choi, Y. Yang, U. Paik, T. Chang, T. J. Dawidczyk, Y. Huang, S. Wang, J. A. Rogers, *Adv. Mater.* **2017**, *29*, 1604989.
- [2] N. Vachicouras, C. M. Tringides, P. B. Campiche, S. P. Lacour, *Extreme Mech. Lett.* **2017**, *15*, 63.
- [3] D. Yang, B. Mosadegh, A. Ainla, B. Lee, F. Khashai, Z. Suo, K. Bertoldi, G. M. Whitesides, *Adv. Mater.* **2015**, *27*, 6323.
- [4] A. Rafsanjani, K. Bertoldi, A. R. Studart, *Sci. Rob.* **2019**, *4*, eaav7874.
- [5] A. Rafsanjani, Y. Zhang, B. Liu, S. M. Rubinstein, K. Bertoldi, *Sci. Rob.* **2018**, *3*, eaar7555.
- [6] D. Goswami, S. Liu, A. Pal, L. G. Silva, R. V. Martinez, *Adv. Funct. Mater.* **2019**, *29*, 1808713.
- [7] S. Janbaz, F. S. L. Bobbert, M. J. Mirzaali, A. A. Zadpoor, *Mater. Horiz.* **2019**, *6*, 1138.
- [8] S. Zhang, A. M. Bellinger, D. L. Gletting, R. Barman, Y.-A. L. Lee, J. Zhu, C. Cleveland, V. A. Montgomery, L. Gu, L. D. Nash, D. J. Maitland, R. Langer, G. Traverso, *Nat. Mater.* **2015**, *14*, 1065.
- [9] S. Babaei, S. Pajovic, A. R. Kirtane, J. Shi, E. Caffarel-Salvador, K. Hess, J. E. Collins, S. Tamang, A. V. Wahane, A. M. Hayward, H. Mazdiyasn, R. Langer, G. Traverso, *Sci. Transl. Med.* **2019**, *11*, eaau8581.
- [10] A. Rafsanjani, D. Pasini, *Extreme Mech. Lett.* **2016**, *9*, 291.
- [11] Y. Tang, G. Lin, S. Yang, Y. K. Yi, R. D. Kamien, J. Yin, *Adv. Mater.* **2017**, *29*, 1604262.
- [12] H. Fu, K. Nan, W. Bai, W. Huang, K. Bai, L. Lu, C. Zhou, Y. Liu, F. Liu, J. Wang, M. Han, Z. Yan, H. Luan, Y. Zhang, Y. Zhang, J. Zhao, X. Cheng, M. Li, J. W. Lee, Y. Liu, D. Fang, X. Li, Y. Huang, Y. Zhang, J. A. Rogers, *Nat. Mater.* **2018**, *17*, 268.
- [13] D.-G. Hwang, M. D. Bartlett, *Sci. Rep.* **2018**, *8*, 3378.
- [14] Y. Yang, M. A. Dias, D. P. Holmes, *Phys. Rev. Mater.* **2018**, *2*, 110601.
- [15] A. Rafsanjani, L. Jin, B. Deng, K. Bertoldi, *Proc. Natl. Acad. Sci. USA* **2019**, *116*, 8200.
- [16] A. Rafsanjani, K. Bertoldi, *Phys. Rev. Lett.* **2017**, *118*, 084301.
- [17] P. Celli, C. McMahan, B. Ramirez, A. Bauhofer, C. Naify, D. Hofmann, B. Audoly, C. Daraio, *Soft Matter* **2018**, *14*, 9744.

- [18] Y. Zhang, Z. Yan, K. Nan, D. Xiao, Y. Liu, H. Luan, H. Fu, X. Wang, Q. Yang, J. Wang, W. Ren, H. Si, F. Liu, L. Yang, H. Li, J. Wang, X. Guo, H. Luo, L. Wang, Y. Huang, J. A. Rogers, *Proc. Natl. Acad. Sci. USA* **2015**, *112*, 11757.
- [19] F. Wang, X. Guo, J. Xu, Y. Zhang, C. Q. Chen, *J. Appl. Mech.* **2017**, *84*, 061007.
- [20] Y. Cho, J.-H. Shin, A. Costa, T. A. Kim, V. Kunin, J. Li, S. Y. Lee, S. Yang, H. N. Han, I.-S. Choi, D. J. Srolovitz, *Proc. Natl. Acad. Sci. USA* **2014**, *111*, 17390.
- [21] Y. Tang, G. Lin, L. Han, S. Qiu, S. Yang, J. Yin, *Adv. Mater.* **2015**, *27*, 7181.
- [22] V. Kunin, S. Yang, Y. Cho, P. Deymier, D. J. Srolovitz, *Extreme Mech. Lett.* **2016**, *6*, 103.
- [23] K. Billon, I. Zampetakis, F. Scarpa, M. Ouisse, E. Sadoulet-Reboul, M. Collet, A. Perriman, A. Hetherington, *Compos. Struct.* **2017**, *160*, 1042.
- [24] Y. Tang, J. Yin, *Extreme Mech. Lett.* **2017**, *12*, 77.
- [25] R. Gatt, L. Mizzi, J. I. Azzopardi, K. M. Azzopardi, D. Attard, A. Casha, J. Briffa, J. N. Grima, *Sci. Rep.* **2015**, *5*, 8395.
- [26] D. Lu, Y. F. Li, H. Seifi, S. Zhou, Z.-L. Zhao, Y. M. Xie, *Extreme Mech. Lett.* **2018**, *19*, 1.
- [27] H. Seifi, A. R. Javan, A. Ghaedizadeh, J. Shen, S. Xu, Y. M. Xie, *Sci. Rep.* **2017**, *7*, 41183.
- [28] K. K. Dudek, R. Gatt, L. Mizzi, M. R. Dudek, D. Attard, K. E. Evans, J. N. Grima, *Sci. Rep.* **2017**, *7*, 46529.
- [29] L. Fang, J. Li, Z. Zhu, S. Orrego, S. H. Kang, *J. Mater. Res.* **2018**, *33*, 330.
- [30] G. Wang, S. Sun, M. Li, J. Zhou, *Mater. Res. Express* **2019**, *6*, 055802.
- [31] T. C. Shyu, P. F. Damasceno, P. M. Dodd, A. Lamoureux, L. Xu, M. Shlian, M. Shtein, S. C. Glotzer, N. A. Kotov, *Nat. Mater.* **2015**, *14*, 785.

ADVANCED FUNCTIONAL MATERIALS

Supporting Information

for *Adv. Funct. Mater.*, DOI: 10.1002/adfm.201906711

Programmable Hierarchical Kirigami

Ning An, August G. Domel, Jinxiong Zhou, Ahmad Rafsanjani, and Katia Bertoldi**

**Supplementary Information for
Programmable Hierarchical Kirigami**

Ning An^{1,2,†}, August G. Domel^{1,†}, Jinxiong Zhou²,
Ahmad Rafsanjani^{1,3,*}, and Katia Bertoldi^{1,4,5,*}

¹*Harvard John A. Paulson School of Engineering and Applied Sciences,
Harvard University, Cambridge, Massachusetts 02138, USA*

²*State Key Laboratory for Strength and Vibration
of Mechanical Structures and School of Aerospace,
Xi'an Jiaotong University, Xi'an 710049, People's Republic of China*

³*Department of Materials, ETH Zürich, 8093 Zürich, Switzerland*

⁴*Kavli Institute, Harvard University,
Cambridge, Massachusetts 02138, USA*

⁵*Wyss Institute for Biologically Inspired Engineering,
Harvard University, Cambridge, Massachusetts 02138, USA and*

[†]*N.A. and A.D. contributed equally to this work.*

(Dated: October 12, 2019)

*Correspondence to ahmad.rafsanjani@mat.ethz.ch and bertoldi@seas.harvard.edu

I. EXPERIMENTS

a. Fabrication The surfaces considered in this study are fabricated from thin polyester plastic sheets (McMaster-Carr, Elmhurst, IL) with thickness $t = 101.6 \mu\text{m}$. The material properties of the plastic sheets used in this study are characterized by performing uniaxial tensile tests with a uniaxial testing machine (Instron 5969) equipped with a 500 N load cell. Strips with a width of 10 mm and gauge length of 250 mm are fully clamped at both ends using pneumatic grippers and stretched with a strain rate of 0.1 min^{-1} up to a strain $\varepsilon = 0.2$. The stress-strain curve reported in Figure S1 indicates that the polyester plastic sheets are characterized by a Young's modulus of 5.17 GPa. Moreover, their corresponding true plastic strain ε_{tp} versus true stress σ_t is reported in Table S1 up to the fully plastic region.

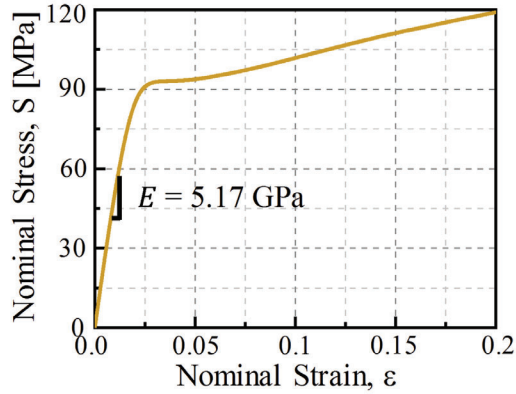


Figure S1: Stress-strain response of the polyester plastic sheet under uniaxial tension.

Kirigami samples consisting of 2×6 unit cells are manufactured out of these plastic sheets using a commercial laser cutter (Universal Laser Systems, Scottsdale, AZ). In all of our samples, the characteristic length is $l = 8\text{mm}$ and the laser cutting process results in cuts of width $\simeq 0.25 \text{ mm}$. Since the loading is always applied along the longitudinal direction of

ε_{tp}	0	0.0003	0.0007	0.0014	0.0031	0.0081	0.0482	0.0714	0.0744
σ_t [MPa]	51.70	60.62	69.60	77.46	86.44	94.30	103.28	111.14	112.26

Table S1: True plastic strain (ε_{tp}) versus true stress (σ_t) for the polyester plastic sheet used in this study.

the samples, we build two variants of the *level 2* samples: one with the unit cells oriented as in Figure S2(a) [for which $\gamma = 0^\circ$ - see Figure S2(b)] and one with the the unit cells rotated by 90° [for which $\gamma = 90^\circ$ - see Figure S2(c)].

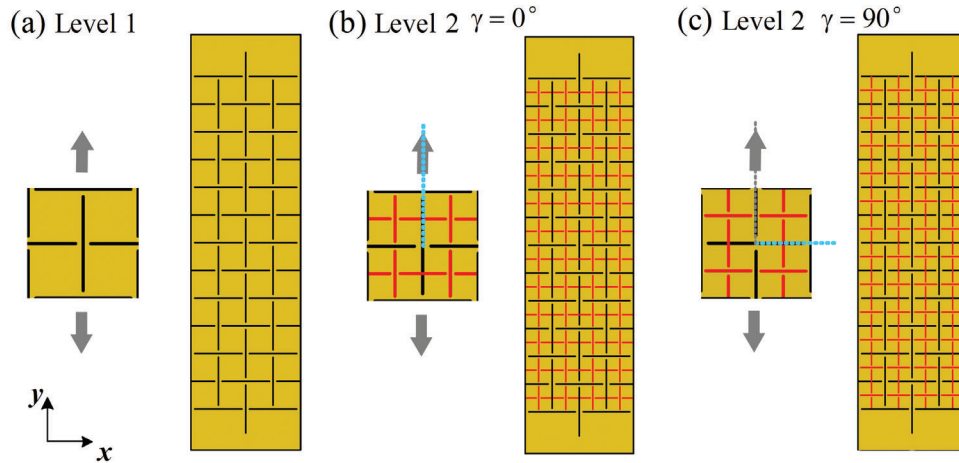


Figure S2: Schematics of our kirigami samples and corresponding unit cells. Each sample consists of 2×6 unit cells. (a) *Level 1* samples. (b) *Level 2* samples with $\gamma = 0^\circ$. (c) *Level 2* samples with $\gamma = 90^\circ$.

b. Testing All samples are stretched uniaxially using a uniaxial testing machine (Instron 5969) equipped with a 500 N load cell (see Figure S3). The tests are conducted under a strain rate of 0.1 min^{-1} and the out-of-plane deformation of the samples is monitored using a digital camera (Sony RX100V) placed in front of the sheets.



Figure S3: Experimental setup. Our kirigami samples are stretched uniaxially using an Instron tensile machine.

II. FINITE ELEMENT SIMULATIONS

To further characterize the mechanical response of the considered kirigami sheets, we also conduct Finite Element (FE) simulations using the commercially available package Abaqus/Standard 2017. In all of our simulations, the models are discretized using 4-node rectangular shell elements with reduced integration (Abaqus element type S4R), and the cuts in the sheets are modeled as thin rectangular slits with a thickness of 0.25 mm (as observed in the physical samples). Moreover, the material behavior of the plastic sheets is captured using an elasto-plastic model (material models *ELASTIC and *PLASTIC in Abaqus) with the properties detailed in Table S1. We note that in all our simulations a typical Poisson’s ratio $\nu = 0.4$ is assumed.

a. Finite size simulations To validate the FE simulations, we first perform full finite size simulations on models comprising an array of 2×6 cells (identical to the samples used in experiments). For these analyses, the lower boundary of the sample is fixed and a vertical displacement is applied to the upper boundary, while the lateral boundaries are assumed to be traction free. The response of the sheets is simulated by conducting dynamic implicit simulations (*DYNAMIC module in Abaqus). To facilitate convergence, we introduce some artificial, numerical damping by setting the parameters $\alpha = -0.41421$, $\beta = 0.5$ and $\gamma = 0.91421$ in the Hiber-Hughes-Taylor time integration algorithm. Moreover, quasi-static conditions are ensured by monitoring the kinetic energy. Finally, to trigger the instability, an imperfection is introduced by applying two opposing small bias forces normal to the sheet plane at the longer side of each cut during the initial step of each simulation. Using this approach, we numerically investigate the response of finite size samples both at *level 1* and at *level 2* and find excellent agreement with the experimental results (see Figure S4, as well as Figure 2 in the main text), confirming the validity of these numerical analyses.

b. Unit cell simulations To reduce the computational cost and ensure the response is not affected by boundary effects, we also consider infinite periodic structures using representative unit cells with suitable periodic boundary conditions. All simulations consist of two steps: (*i*) we first use a linear perturbation analysis (*BUCKLING module in Abaqus) to identify the critical buckling mode; (*ii*) we then introduce a small imperfection ($\simeq 0.001l$) in the form of the critical mode into the mesh to guide the post-buckling analysis. To validate our unit cell simulations, we start by comparing their results to those of the finite

size simulations and experiments. As shown in Figure S4, we find excellent quantitative agreements between all stress-strain curves, with small discrepancies caused by boundary effects.

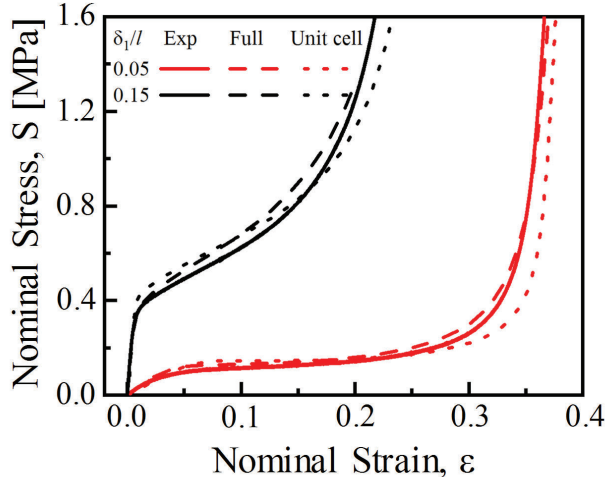


Figure S4: Quantitative comparison between experimental and numerical (full finite size simulations and unit cell simulations) results.

Having verified the validity of our unit cell simulations, we then use them to parametrically investigate the effect of geometric parameters (i.e. δ_1/l and δ_2/l) on the mechanical response of the system. Towards this end, we simulate the response of kirigami unit cells with $\delta_1/l \in [0.0525, 0.15]$ and $\delta_2/l \in [0.0525, 0.1]$. The results of this parametric study are reported in Figures S12-S10. For all the considered kirigami sheets, the mechanical response is initially linear with a sudden departure from linearity as a result of buckling, and then a stiffening region upon further tension. However, it is important to note that the specific characteristics of the stress-strain curves can be significantly tuned by altering δ_1/l and δ_2/l . Specifically, for both the *level 1* sheets and *level 2* systems with $\gamma = 0^\circ$ an increase of δ_1/l (at a fixed δ_2/l) leads to a shorter stress plateau and an earlier hardening region (see Figures S5 and S6). Differently, for the *level 2* systems with $\gamma = 90^\circ$ an increase of δ_1/l does not alter the size of the stress plateau and only shifts its position to larger stresses (see Figure S7). Moreover, we note that for the *level 2* systems with small enough values of δ_1/δ_2 an interesting distinct double-plateau behavior emerges (see Figures S6 and S7) - a clear signature of sequential buckling. For these structures, the first stress plateau is caused by

the out-of-plane buckling of the *level 1* cuts, which gives rise to a pattern similar to that of our *level 1* systems. The second stress plateau is then the result of the out-of-plane buckling of the *level 2* cuts.

Finally, in Figures S8-S10 we report numerical snapshots for both *level 1* and *level 2* structures. The results show that our hierarchical kirigami sheets support a variety of buckling-induced 3D morphologies that can be controlled by tuning δ_1/l , δ_2/l and the applied strain.

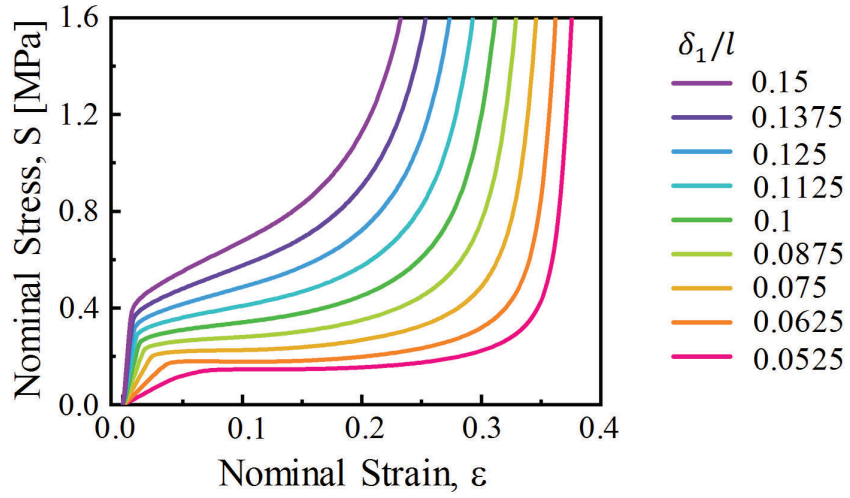


Figure S5: Effect of δ_1/l on the mechanical response of the *level 1* elastoplastic kirigami sheets.

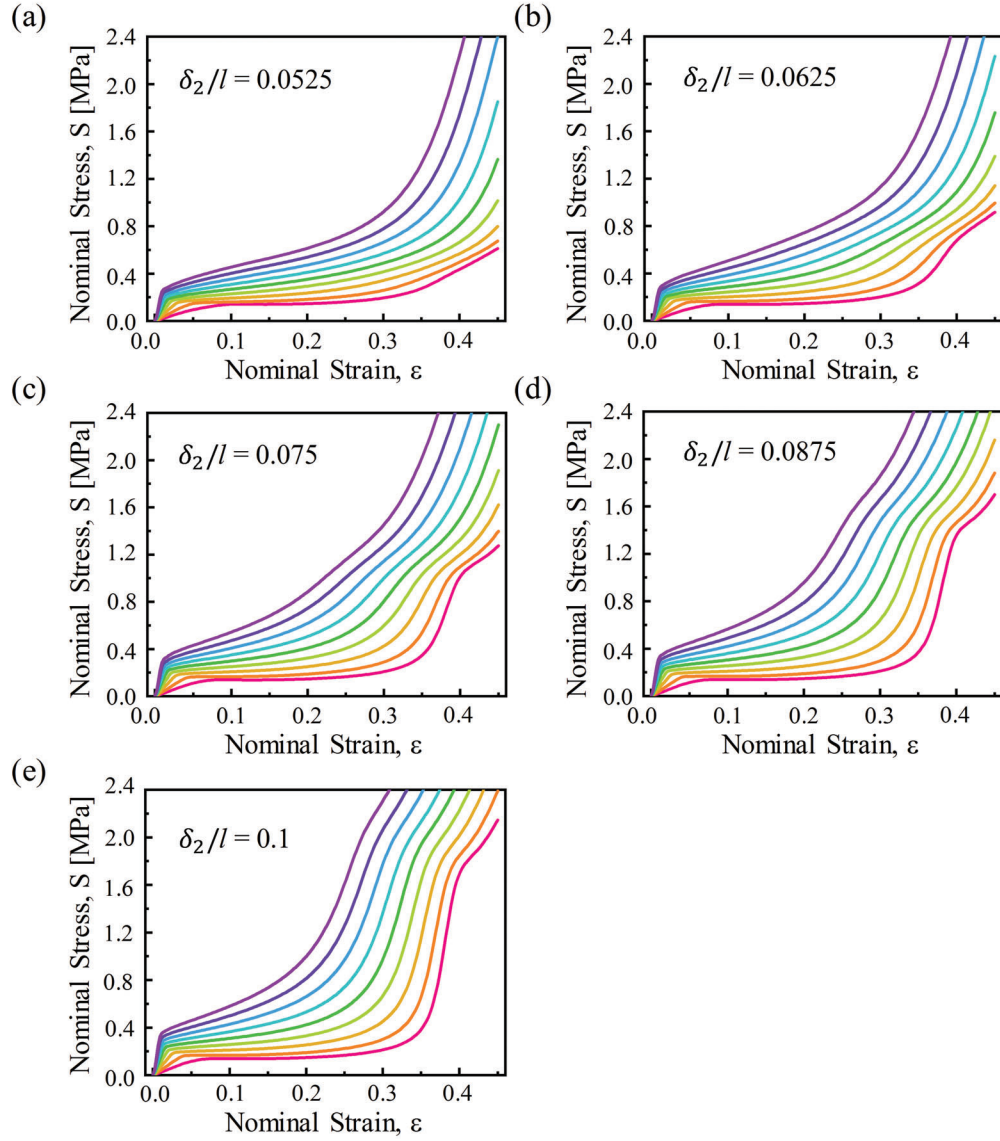


Figure S6: Effect of δ_1/l and δ_2/l on the mechanical response of *level 2* elastoplastic kirigami sheets with $\gamma = 0^\circ$. Note that we are using the same legend as in Figure S5.

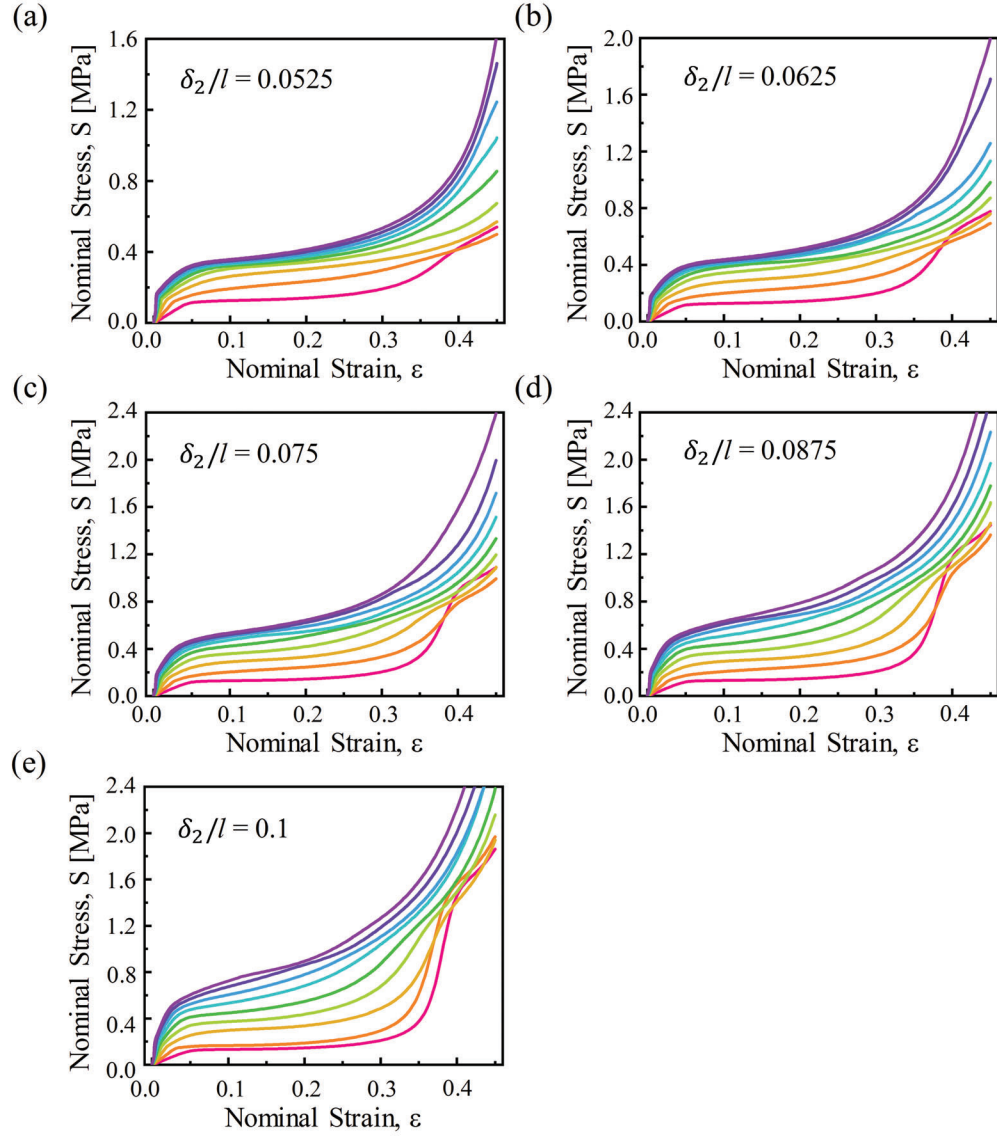


Figure S7: Effect of δ_1/l and δ_2/l on the mechanical response of *level 2* elastoplastic kirigami sheets with $\gamma = 90^\circ$. Note that we are using the same legend as in Figure S5.

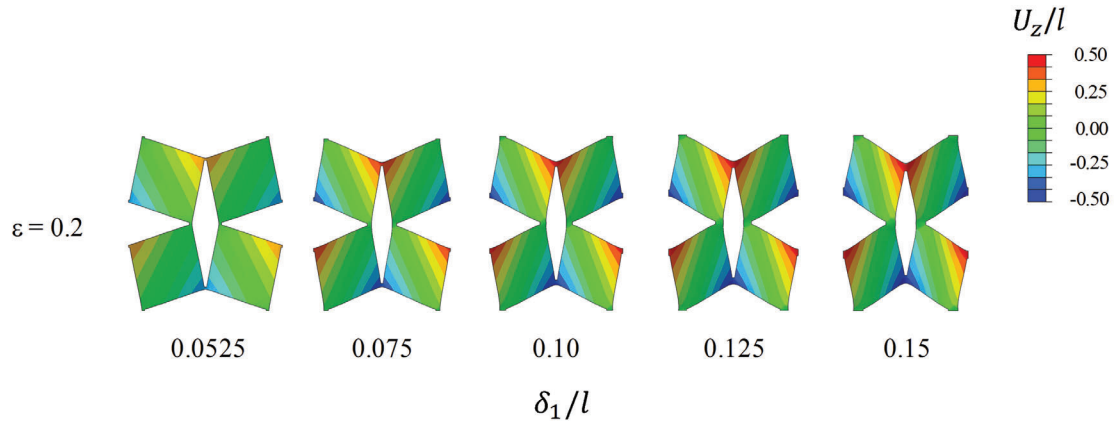


Figure S8: Effect of δ_1/l on the buckled morphology of *level 1* elastoplastic kirigami sheets at $\varepsilon = 0.2$. In the numerical images we show the normalized out-of-plane displacement (U_z) distributions in the deformed configurations.

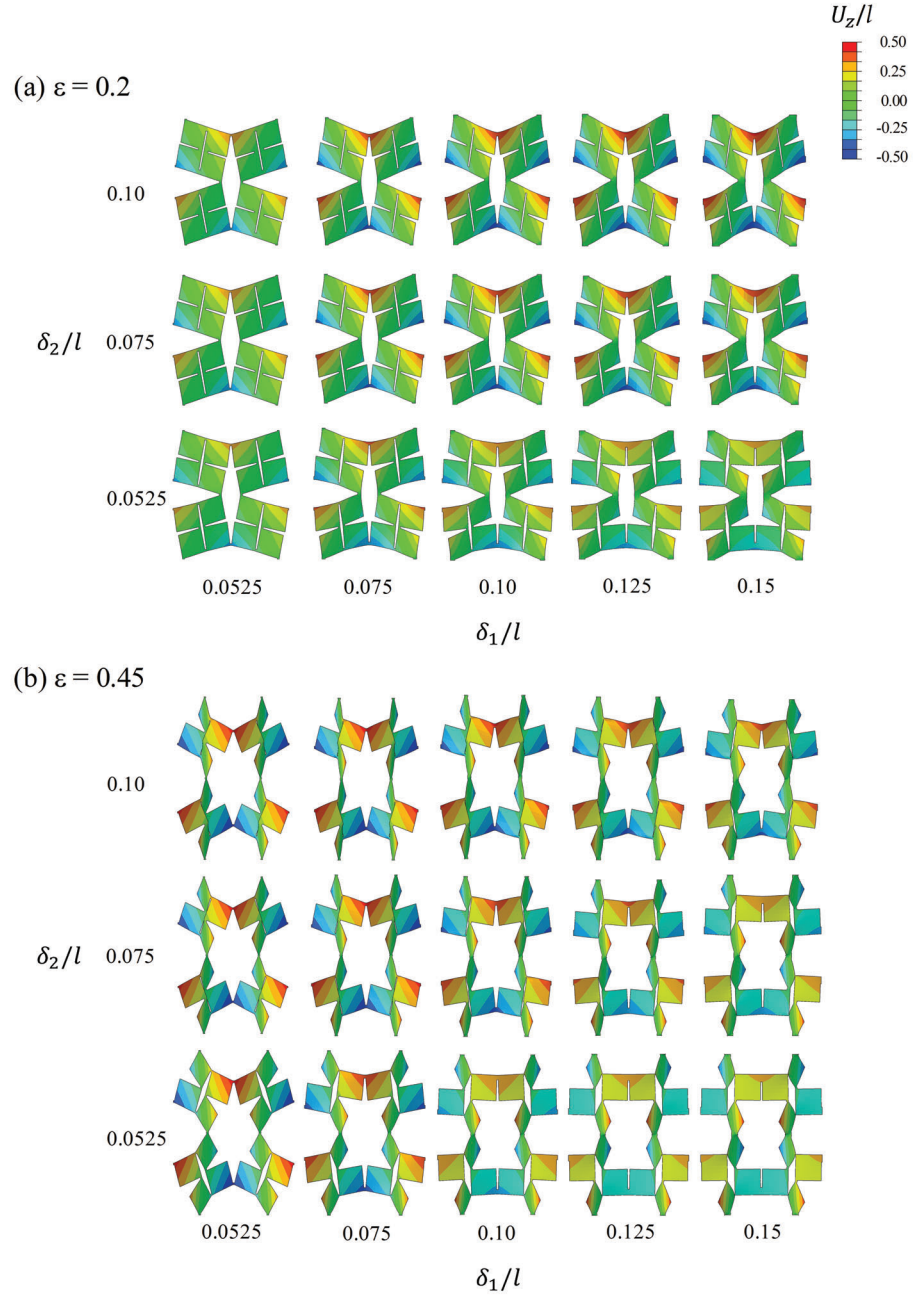


Figure S9: Effect of δ_1/l and δ_2/l on the buckled morphology of *level 2* elastoplastic kirigami sheets with $\gamma = 0^\circ$ at (a) $\varepsilon = 0.2$ and (b) $\varepsilon = 0.45$. In the numerical images we show the normalized out-of-plane displacement (U_z) distributions in the deformed configurations.

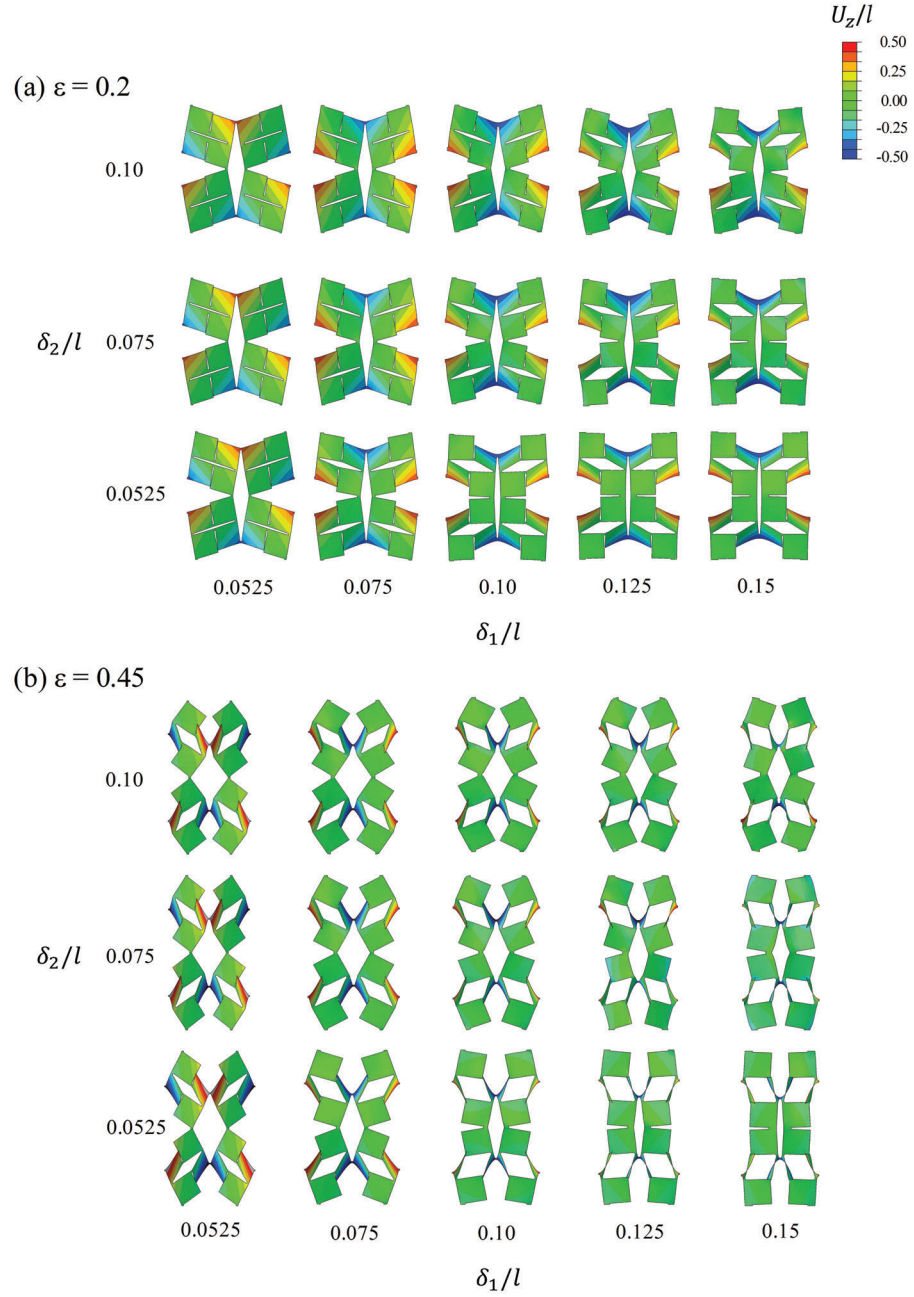


Figure S10: Effect of δ_1/l and δ_2/l on the buckled morphology of *level 2* elastoplastic kirigami sheets with $\gamma = 90^\circ$ at (a) $\varepsilon = 0.2$ and (b) $\varepsilon = 0.45$. In the numerical images we show the normalized out-of-plane displacement (U_z) distributions in the deformed configurations.

A. Additional numerical results

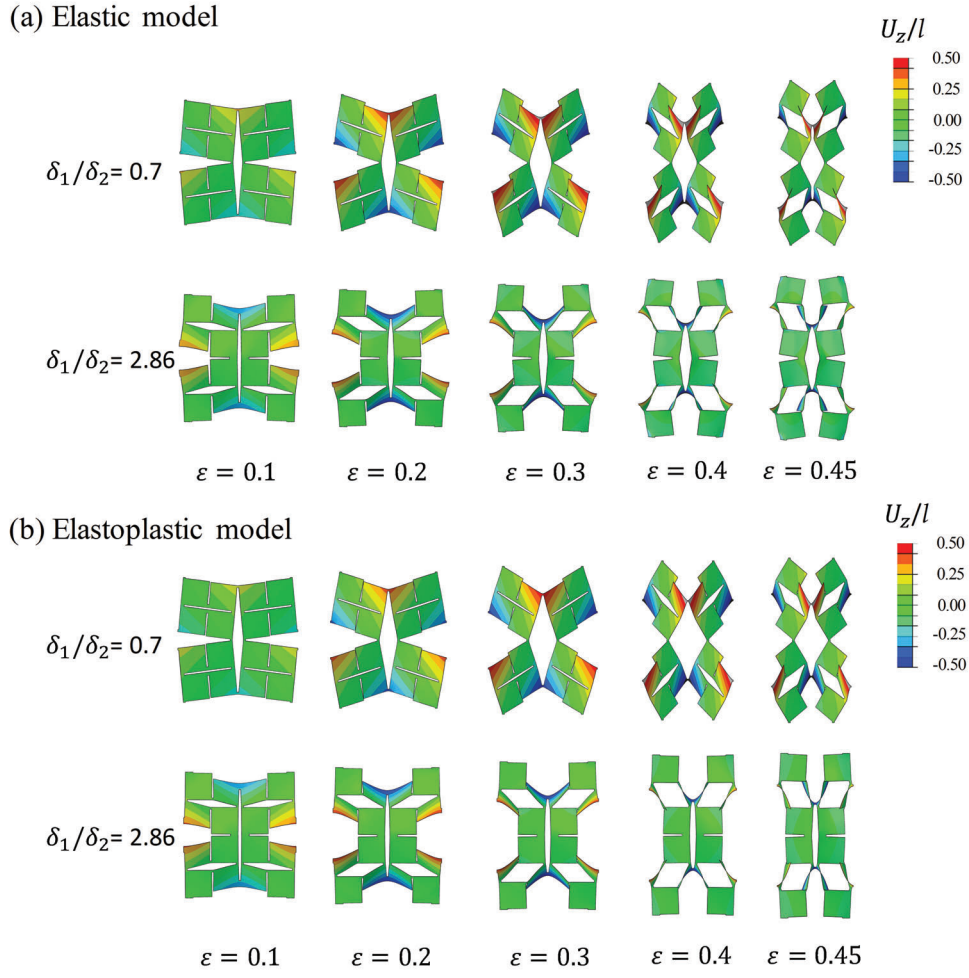


Figure S11: Effect of the material response on the buckled morphology of *level 2* systems characterized by $(\delta_1/l, \delta_2/l) = (0.0525, 0.075)$ and $(0.15, 0.0525)$ for $\gamma = 90^\circ$. (a) Snapshots at different level of applied deformation for purely elastic sheets. (a) Snapshots at different level of applied deformation for elastoplastic sheets. In the numerical images we show the distribution of the normalized out-of-plane displacement (U_z) in the deformed configurations.

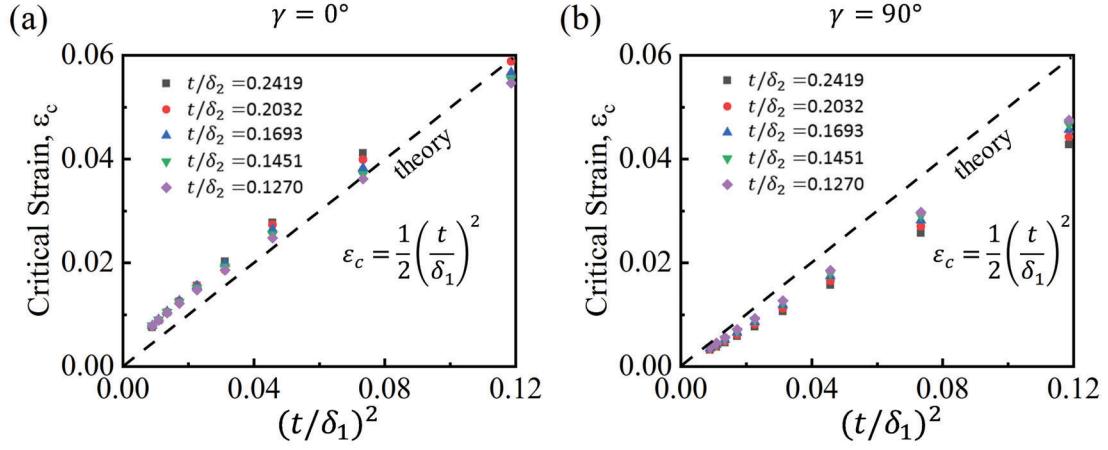


Figure S12: Evolution of critical strain ε_c for *level 2* elastoplastic kirigami sheets as a function of $(t/\delta_1)^2$ for (a) $\gamma = 0^\circ$ and (b) $\gamma = 90^\circ$. The dashed line corresponds to the analytical prediction previously derived for *level 1* patterns, $\varepsilon_c = 0.5(t/\delta_1)^2$ [1].

III. DESIGN OF HETEROGENEOUS KIRIGAMI SHEETS WITH COMPLEX MECHANICAL RESPONSE

Having demonstrated that by carefully controlling the ligament widths generated by both the *level 1* and *level 2* cuts, both the stress-strain behavior and the buckling-induced 3D morphology can be tuned, we now seek to further expand the design space by investigating the response of heterogeneous kirigami surfaces comprising patterns characterized by different geometric parameters. We first focus on the stress-strain response of such heterogeneous sheet and derive a simple and robust strategy to predict their behavior. Then, we explore how to combine different patterns to realize textured surfaces.

A. A Stress-strain response

We start by focusing on heterogeneous surfaces comprising a 1D array of n kirigami patterns connected in series (see Figure S13) and develop a numerical algorithm that takes as input the stress-strain curves of the building blocks obtained via the unit cell simulations and uses them to predict the response of the system.

Toward this end, we start by noting that, upon uniaxial stretching, the state of the i -th building block (characterized by $\delta_1^{(i)}/l$ and $\delta_2^{(i)}/l$) is defined by its (nominal) stress $S^{(i)}$ and strain $\varepsilon^{(i)}$, so that its stored elastic energy can be calculated as

$$u^{(i)}(\varepsilon^{(i)}) = \int_0^{\varepsilon^{(i)}} S^{(i)}(\tilde{\varepsilon}) d\tilde{\varepsilon} \quad (\text{S1})$$

When the total displacement applied to the system, $\varepsilon L = \sum_{i=1}^n \varepsilon^{(i)} L^{(i)}$ ($L^{(i)}$ denoting the length of the i -th building block and $L = \sum_{i=1}^n L^{(i)}$) is controlled, its response is characterized by $n-1$ variables $\varepsilon^{(1)}, \dots, \varepsilon^{(n-1)}$ and the constraint

$$\varepsilon^{(n)} = \frac{\varepsilon L - \sum_{i=1}^{n-1} \varepsilon^{(i)} L^{(i)}}{L^{(n)}} \quad (\text{S2})$$

To determine the equilibrium configuration, we first define the density of the total strain energy stored in the system, ψ , which is given by the sum of the strain energies of individual

building blocks:

$$\psi(\varepsilon^{(1)}, \dots, \varepsilon^{(n)}) = \frac{\sum_{i=1}^n L^{(i)} \int_0^{\varepsilon^{(i)}} S^{(i)}(\tilde{\varepsilon}) d\tilde{\varepsilon}}{L} \quad (\text{S3})$$

and use Equation (S2) to express the energy density in terms of $n-1$ variables,

$$\tilde{\psi}(\varepsilon^{(1)}, \dots, \varepsilon^{(n-1)}) = \frac{\sum_{i=1}^{n-1} L^{(i)} \int_0^{\varepsilon^{(i)}} S^{(i)}(\tilde{\varepsilon}) d\tilde{\varepsilon}}{L} + \frac{L^{(n)} \int_0^{\varepsilon^{(n)}} S^{(n)}(\tilde{\varepsilon}) d\tilde{\varepsilon}}{L} \quad (\text{S4})$$

The equilibrium states for the system are then found as

$$\frac{\partial \tilde{\psi}}{\partial \varepsilon^{(i)}} = S^{(i)}(\varepsilon^{(i)}) - S^{(n)}(\varepsilon^{(n)}) = 0, \quad \text{for } i = 1, \dots, n-1. \quad (\text{S5})$$

As expected, Equation S5 ensures that the nominal stress is the same in all n building blocks connected in series when subjected to uniaxial tension.

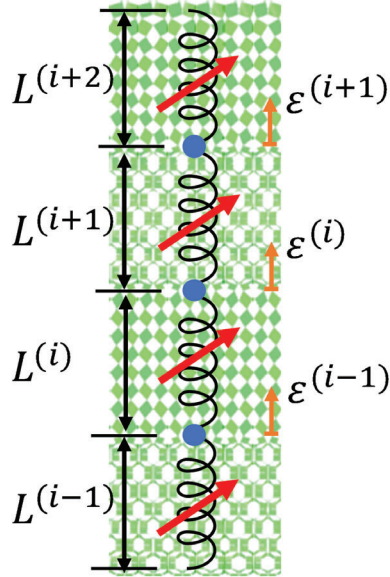


Figure S13: Schematic of our model comprising 1D array of nonlinear springs

To simulate the response of a heterogeneous kirigami surface, we first fit the numerically obtained stress-strain curves of the corresponding individual build blocks with cubic splines. We then solve the system of non-linear equations Equation S5 (together with Equation S2) numerically for increasing values of the applied strain ε using the trust-region-dogleg

algorithm implemented in Matlab[2, 3]. In addition, we note that by using Equation S4 we can also determine the evolution of the total strain energy density stored in the system, $\tilde{\psi}$, as a function of the strains of $n-1$ building blocks, for increasing values of applied strain ε . Finally, by finding the minimum total strain energy density, we can further calculate the strains of each building block as a function of the evolution of the total strain.

a. Results We can use all of the reported stress-strain curves in Figures S5-S7 to predict the response of any combination of heterogeneous surfaces comprising multiple building blocks. To test the relevance of our model, we first focus on a heterogeneous surface comprising two building blocks composed of 2×5 unit cells (so that $L^{(1)} = L^{(2)} = 10l$) characterized by $\delta_1^{(1)}/l = 0.0525$ (*level 1*) and $\delta_1^{(2)}/l = 0.15$, $\delta_2^{(2)}/l = 0.0525$, and $\gamma^{(2)} = 90^\circ$ and compare the prediction of our model to both experimental and FE results. As shown in Figure 6 of the main text, we find excellent agreement between the three sets of data, confirming the validity of our model. Next, we use our model to efficiently explore the design space. To this end, in Figures S14 and S15 we report the results of different heterogeneous surfaces comprising 2 building blocks. One building block is fixed to be a *level 1* system with $\delta_1^{(1)}/l = 0.0525$, while the other one is one of *level 2* systems with $\delta_1^{(2)}/l \in [0.0525, 0.15]$ and $\delta_2^{(2)}/l \in [0.0525, 0.1]$. It can be seen from Figures S14, S15 and Figure 7 of the main text that by creating the heterogeneous surfaces, we obtain much more tunability and programmability of the stress-strain responses for the hierarchical kirigami surfaces than just a single surface alone. In particular, we can tune the length of the stress plateau before final stiffening as well as generate double-plateau deformation behaviors.

Based on these results, we find that heterogeneous surfaces with double stress-plateau can be realized by connecting building blocks with (*i*) plateau stresses that are separate enough and (*ii*) having almost zero stiffness immediately after buckling.

While in Figures S14 and S15 we have focused on heterogeneous surfaces comprising two building blocks, our approach can be readily extended to design system with arbitrary number of blocks. For example, in Figure S16 we consider a heterogeneous surface comprising three building blocks composed of 2×5 unit cells (so that $L^{(1)} = L^{(2)} = L^{(3)} = 10l$) characterized by $\delta_1^{(1)}/l = 0.0525$ (*level 1*) and $\delta_1^{(2)}/l = 0.1$, $\delta_2^{(2)}/l = 0.0525$, $\gamma^{(2)} = 90^\circ$ and $\delta_1^{(3)}/l = 0.4$, $\delta_2^{(3)}/l = 0.0525$, and $\gamma^{(3)} = 90^\circ$ [see Figures S16(a) and S16(b)]. While all these three building blocks are characterized by a stress-strain curve with a single plateau, it is interesting to note that our model results indicate that three stress-plateaus emerge when

they are combined [see Figures S16(c) and S16(d)]. The sequential buckling behavior of the heterogeneous surface is also apparent in S16(e), where we report the evolution of $\varepsilon^{(1)}$, $\varepsilon^{(2)}$ and $\varepsilon^{(3)}$ as a function of the applied strain ε . As ε increases, ε_1 increases first; ε_2 eventually increases only after ε_1 has plateaued and finally ε_3 increases after ε_2 has plateaued. We also note that by altering the length ratio of the building blocks ($L^{(2)}/L^{(1)}$ and $L^{(3)}/L^{(1)}$), we are able to further tune the critical strain where the stress plateau will occur as well as the length of the stress plateau [see Figure S16(f)].

B. B Textured surfaces

While so far we have looked at different building blocks arranged in series, we now explore the possibility of arranging them in 2D space. We note that if we arrange arbitrary kirigami patterns in parallel they strongly affect each other, so that the response of the heterogeneous system cannot be predicted only based on the behavior of the building blocks (see Figure S17). To overcome this issue, we combine two different patterns with similar stress-strain behavior but distinct deformation modes into regions of the 2D space to define a target image. This results in heterogeneous surfaces with the same stress-strain response of the building blocks, but capable of revealing information (in form of an image) as soon as the system is subjected to uniaxial stretching to induce out-of-plane buckling.

To realize texture surfaces; two conditions should be met: (i) the stress-strain responses of the two building blocks should be very close to each other; (ii) the deformed patterns of the two building blocks should be as different as possible. To demonstrate the concept we focus on two pairs of unit cells: (i) Pair 1 which comprises building block #1 characterized by $\delta_1^{(1)}/l = 0.1375$, $\delta_2^{(1)}/l = 0.075$ and $\gamma^{(1)} = 0^\circ$, and building block #2 characterized by $\delta_1^{(2)}/l = 0.15$, $\delta_2^{(2)}/l = 0.075$ and $\gamma^{(2)} = 90^\circ$; (ii) Pair 2 which comprises building block #1 characterized by $\delta_1^{(1)}/l = 0.125$, $\delta_2^{(1)}/l = 0.0525$ and $\gamma^{(1)} = 0^\circ$, and building block #2 characterized by $\delta_1^{(2)}/l = 0.15$, $\delta_2^{(2)}/l = 0.0525$ and $\gamma^{(2)} = 90^\circ$. In Figures S18-S25 we show additional experimental results obtained for these two pairs of building blocks.

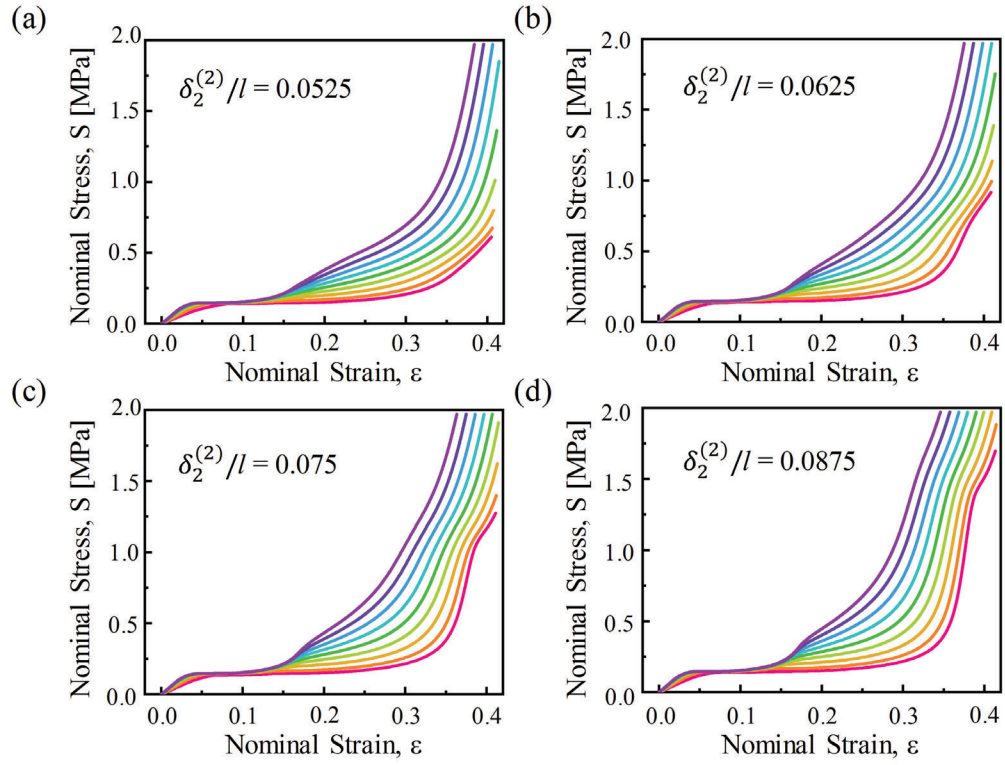


Figure S14: Mechanical response of the heterogeneous surfaces comprising a *level 1* system (with $\delta_1^{(1)}/l = 0.0525$) and a *level 2* system (with $\gamma^{(2)} = 0^\circ$ and with various combinations of $\delta_1^{(2)}/l$ and $\delta_2^{(2)}/l$ values using the same legend as in Figure S5).

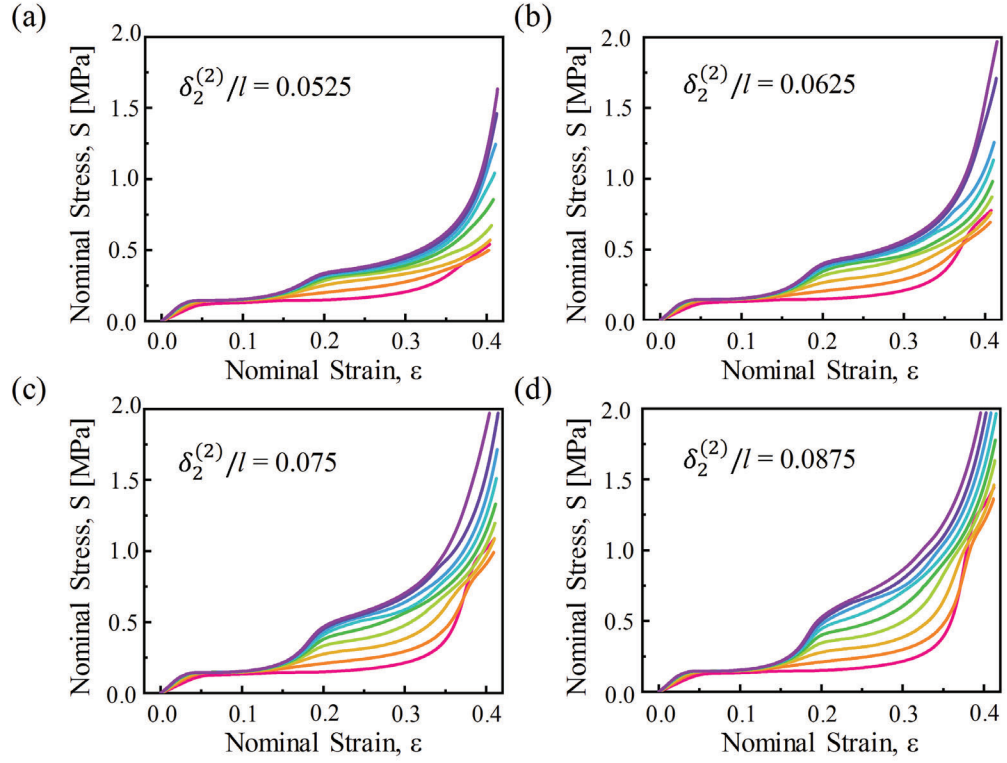


Figure S15: Mechanical response of the heterogeneous surfaces comprising a *level 1* system (with $\delta_1^{(1)}/l = 0.0525$) and a *level 2* system (with $\gamma^{(2)} = 90^\circ$ and with various combinations of $\delta_1^{(2)}/l$ and $\delta_2^{(2)}/l$ values using the same legend as in Figure S5).

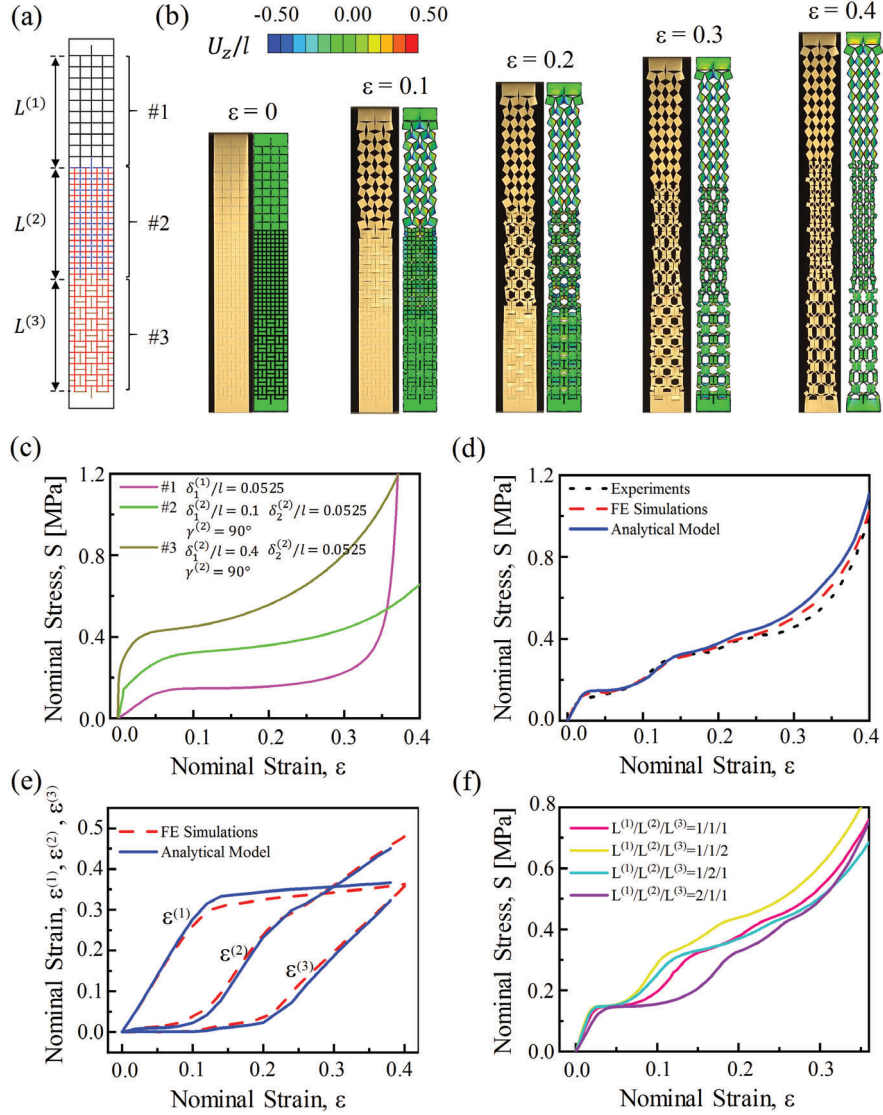


Figure S16: Response of a heterogeneous kirigami surface comprising 3 building blocks. (a) Schematic of the heterogeneous surface. (b) Experimental and numerical snapshots of the heterogeneous kirigami surface at different levels of applied strain. (c) Stress-strain response of the three individual building blocks. (d) Stress-strain response of the combined heterogeneous surface as predicted by our analytical model (solid line) compared to experiments (dotted line) and FE simulations (dashed line). (e) Evolution of $\epsilon^{(1)}$, $\epsilon^{(2)}$, and $\epsilon^{(3)}$ as a function of the applied strain ϵ . (f) Stress-strain response of the combined heterogeneous surface with building blocks characterized by different length.

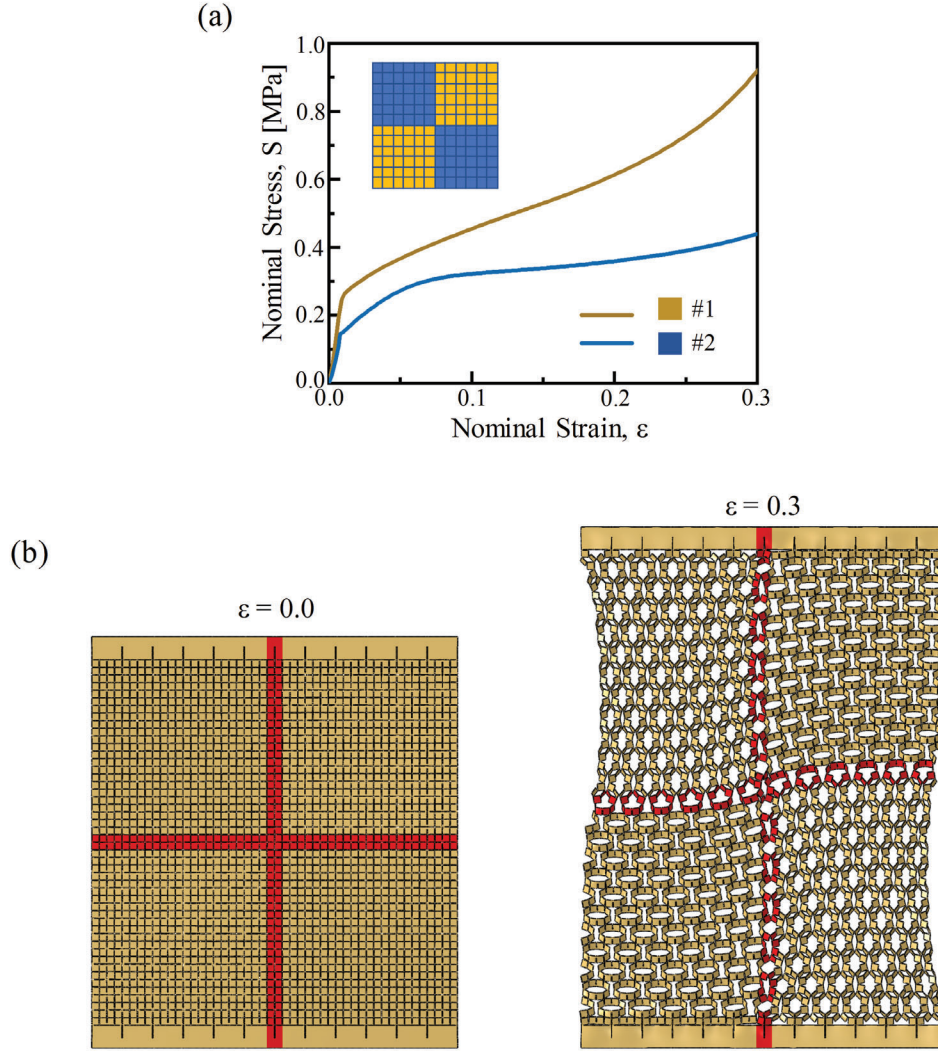


Figure S17: (a) Stress-strain response of two kirigami patterns characterized by $\delta_1^{(2)}/l = 0.15$, $\delta_2^{(2)}/l = 0.0525$, and $\gamma^{(2)} = 0^\circ$ and $\delta_1^{(2)}/l = 0.1$, $\delta_2^{(2)}/l = 0.0525$, and $\gamma^{(2)} = 90^\circ$. (b) Numerical snapshots of the heterogeneous kirigami surface at $\varepsilon = 0.0$ and $\varepsilon = 0.3$. The distortion is due to coupling between the building blocks arranged in parallel.

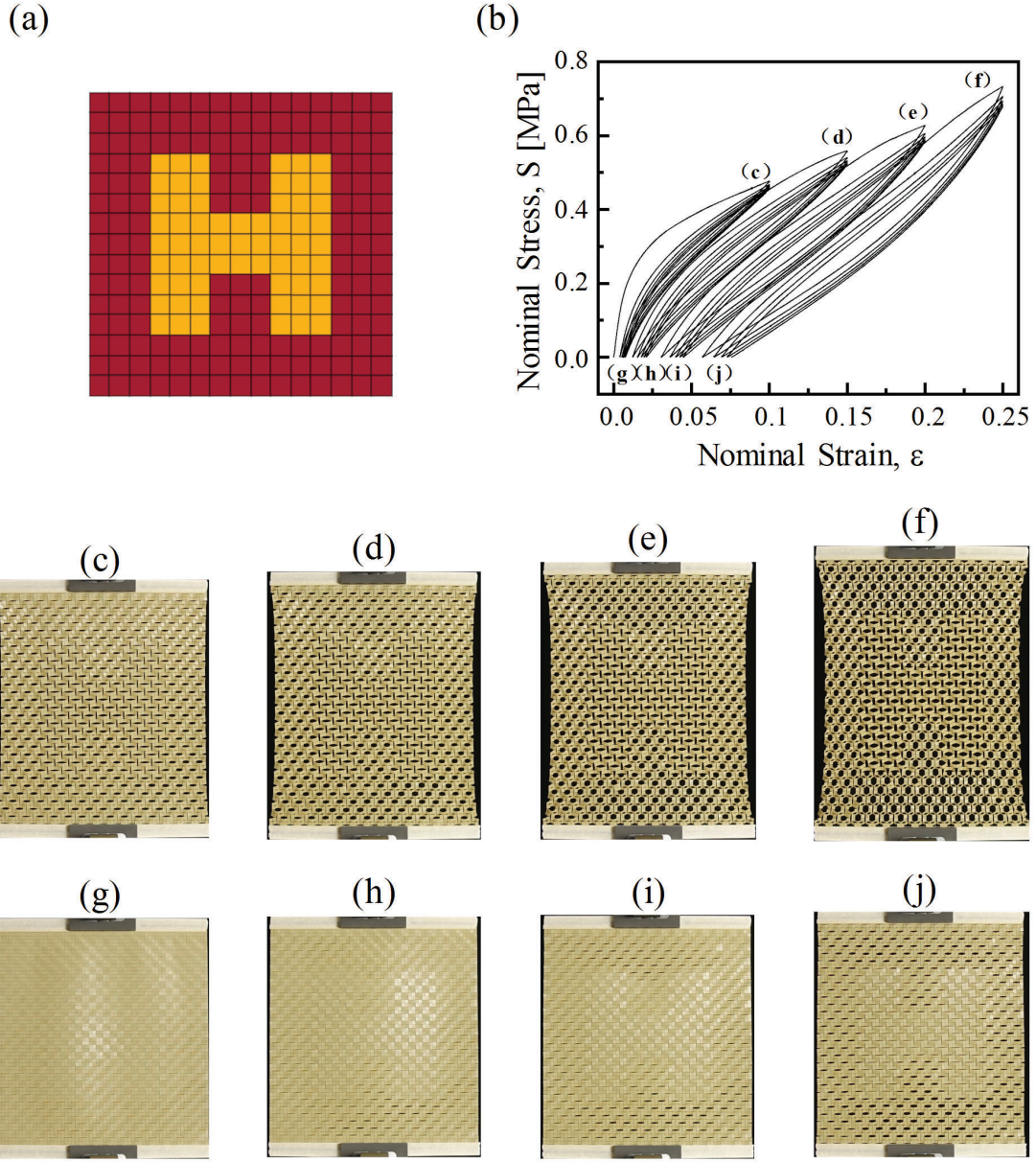


Figure S18: (a) Schematic of a kirigami textured surface with embedded an H. The yellow region is characterized by $\delta_1^{(1)}/l = 0.1375$, $\delta_2^{(1)}/l = 0.075$ and $\gamma^{(1)} = 0^\circ$ and the red region is characterized by $\delta_1^{(2)}/l = 0.15$, $\delta_2^{(2)}/l = 0.075$ and $\gamma^{(2)} = 90^\circ$. (b) Stress-strain response recorded during a cyclic test. (c-j) Experimental images captured right after the applied strain is increased to $\varepsilon = 0.1, 0.15, 0.2$ and 0.25 and then the load is dropped to zero.

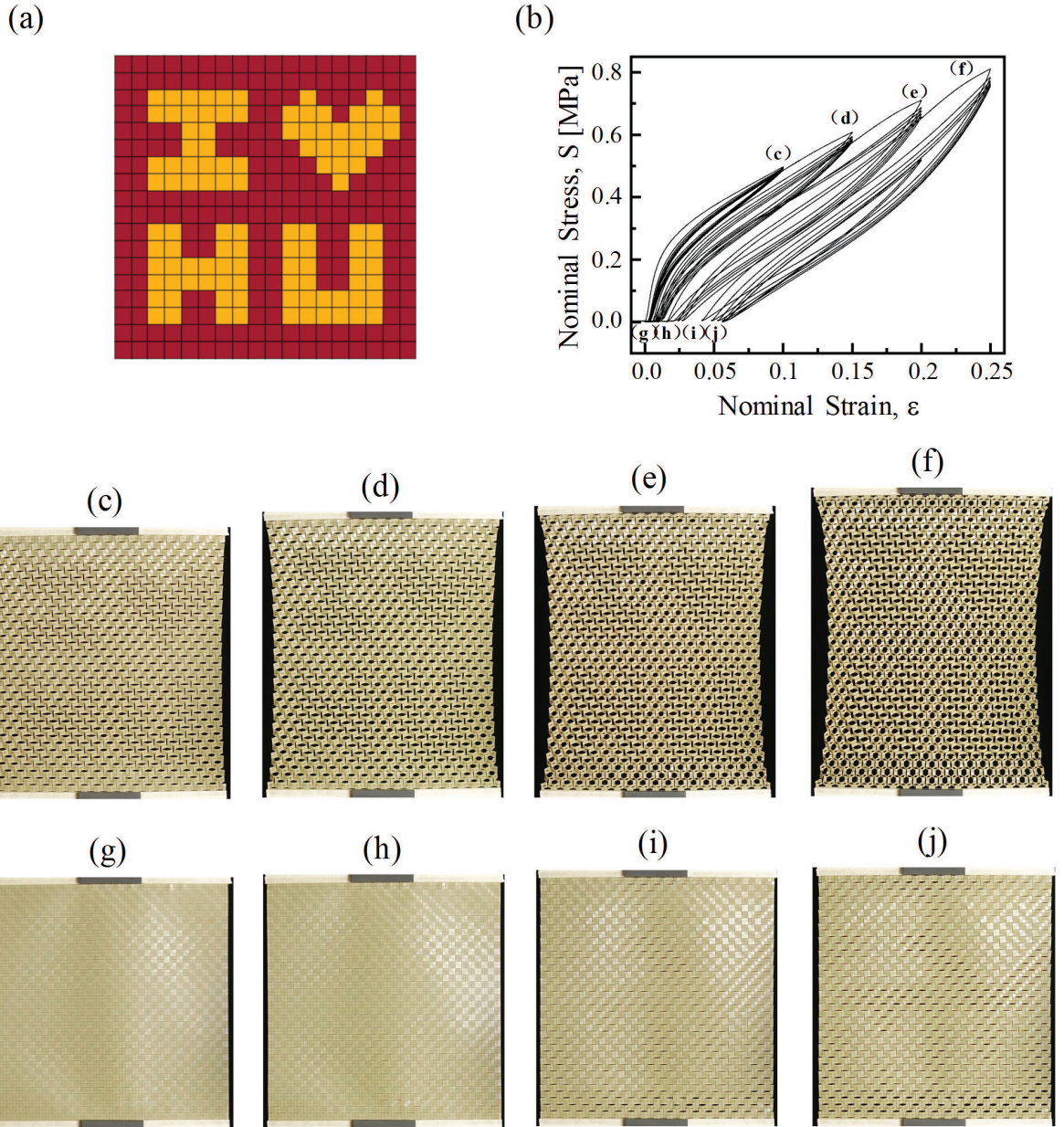


Figure S19: (a) Schematic of a kirigami textured surface with embedded "IHU" shape. The yellow region is characterized by $\delta_1^{(1)}/l = 0.1375$, $\delta_2^{(1)}/l = 0.075$ and $\gamma^{(1)} = 0^\circ$ and the red region is characterized by $\delta_1^{(2)}/l = 0.15$, $\delta_2^{(2)}/l = 0.075$ and $\gamma^{(2)} = 90^\circ$. (b) Stress-strain response recorded during a cyclic test. (c-j) Experimental images captured right after the applied strain is increased to $\epsilon = 0.1, 0.15, 0.2$ and 0.25 and then the load is dropped to zero.

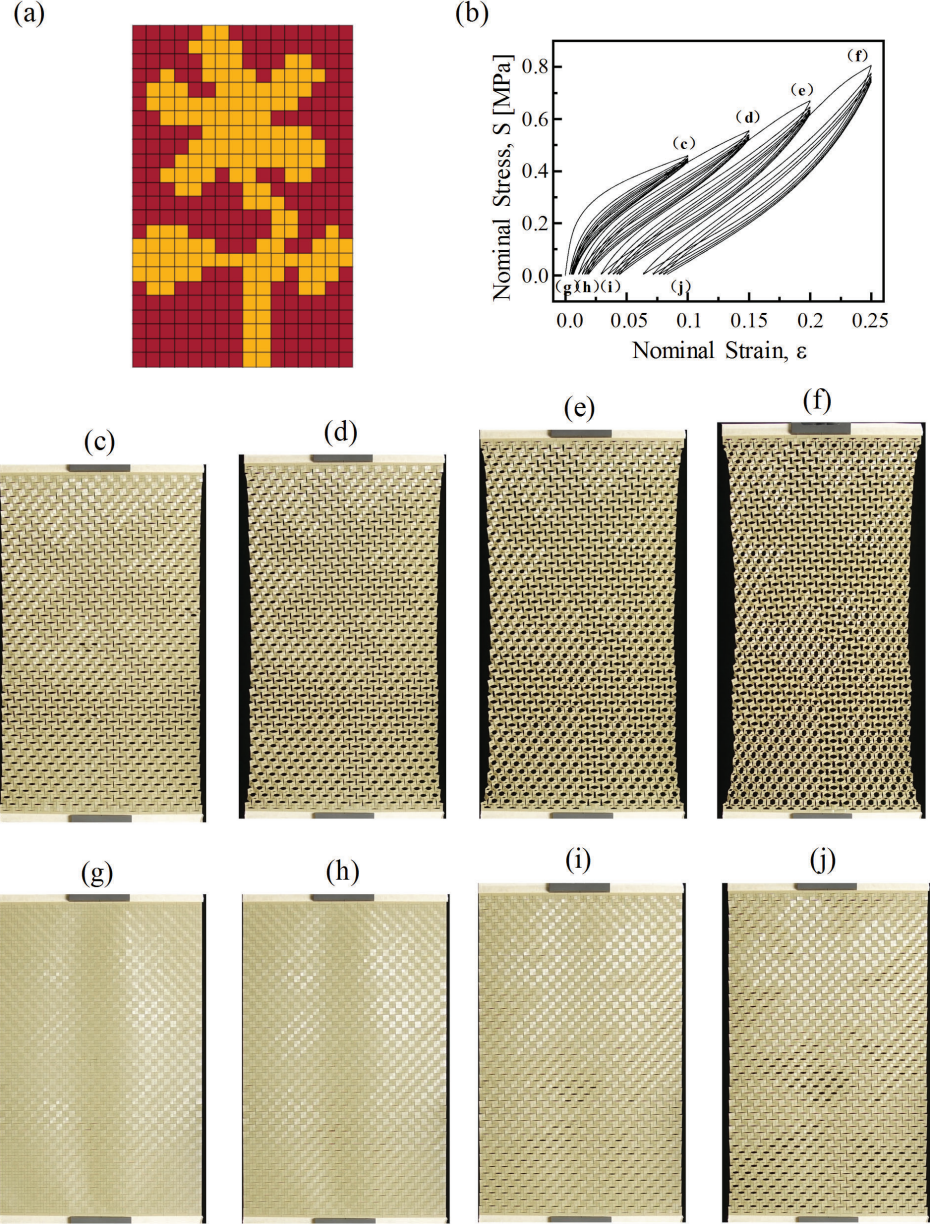


Figure S20: (a) Schematic of a kirigami textured surface with embedded a flower. The yellow region is characterized by $\delta_1^{(1)}/l = 0.1375$, $\delta_2^{(1)}/l = 0.075$ and $\gamma^{(1)} = 0^\circ$ and the red region is characterized by $\delta_1^{(2)}/l = 0.15$, $\delta_2^{(2)}/l = 0.075$ and $\gamma^{(2)} = 90^\circ$. (b) Stress-strain response recorded during a cyclic test. (c-j) Experimental images captured right after the applied strain is increased to $\epsilon = 0.1, 0.15, 0.2$ and 0.25 and then the load is dropped to zero.

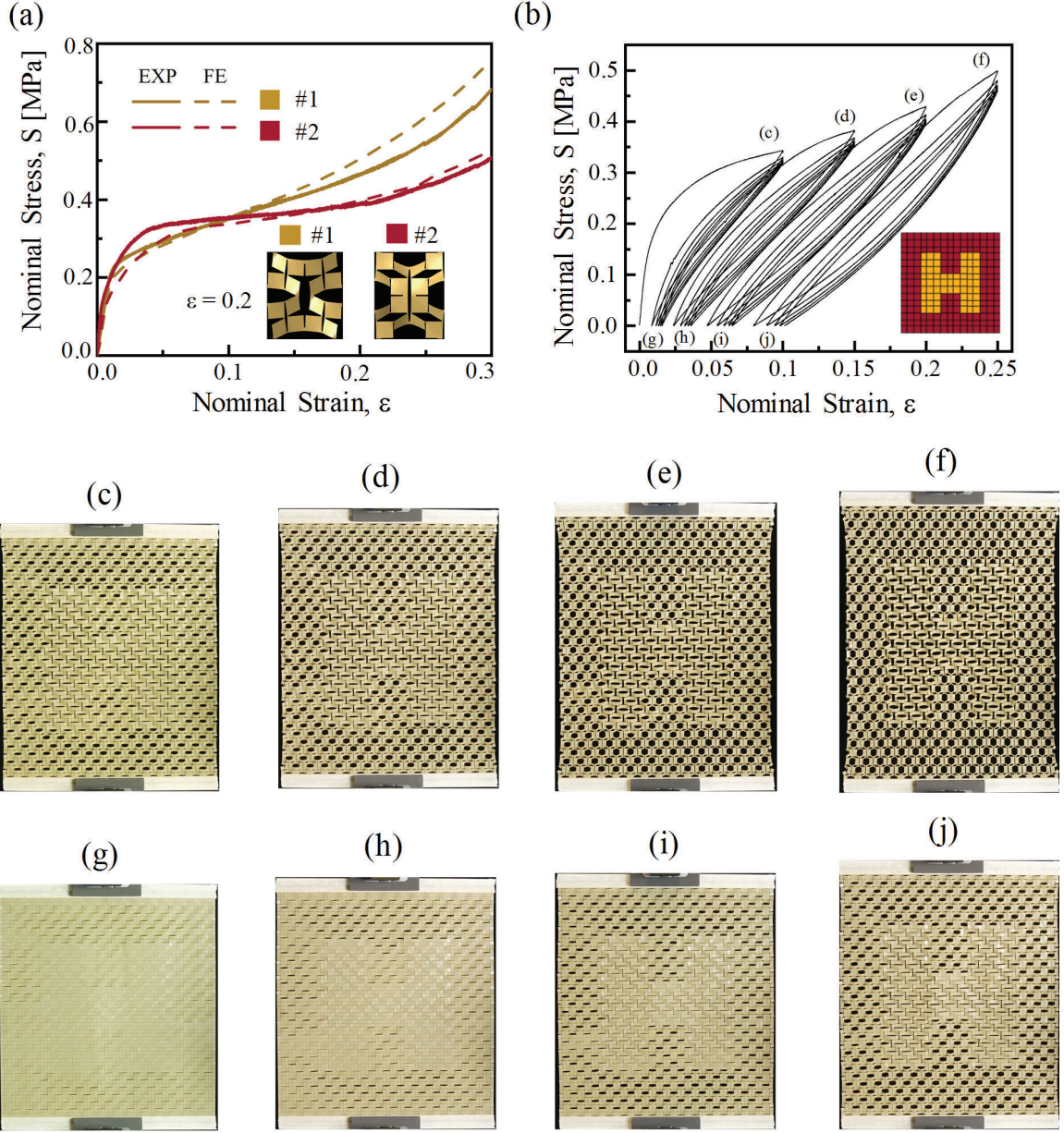


Figure S21: Design of a kirigami textured surface with embedded an H. (a) Stress-strain response of the two unit cells with deformed patterns at a strain of 0.2. #1 is characterized by $\delta_1^{(1)}/l = 0.125$, $\delta_2^{(1)}/l = 0.0525$ and $\gamma^{(1)} = 0^\circ$, and #2 is characterized by $\delta_1^{(2)}/l = 0.15$, $\delta_2^{(2)}/l = 0.0525$ and $\gamma^{(2)} = 90^\circ$. (b) Stress-strain response recorded during a cyclic test. (c-j) Experimental images captured right after the applied strain is increased to $\epsilon = 0.1, 0.15, 0.2$ and 0.25 and then the load is dropped to zero.

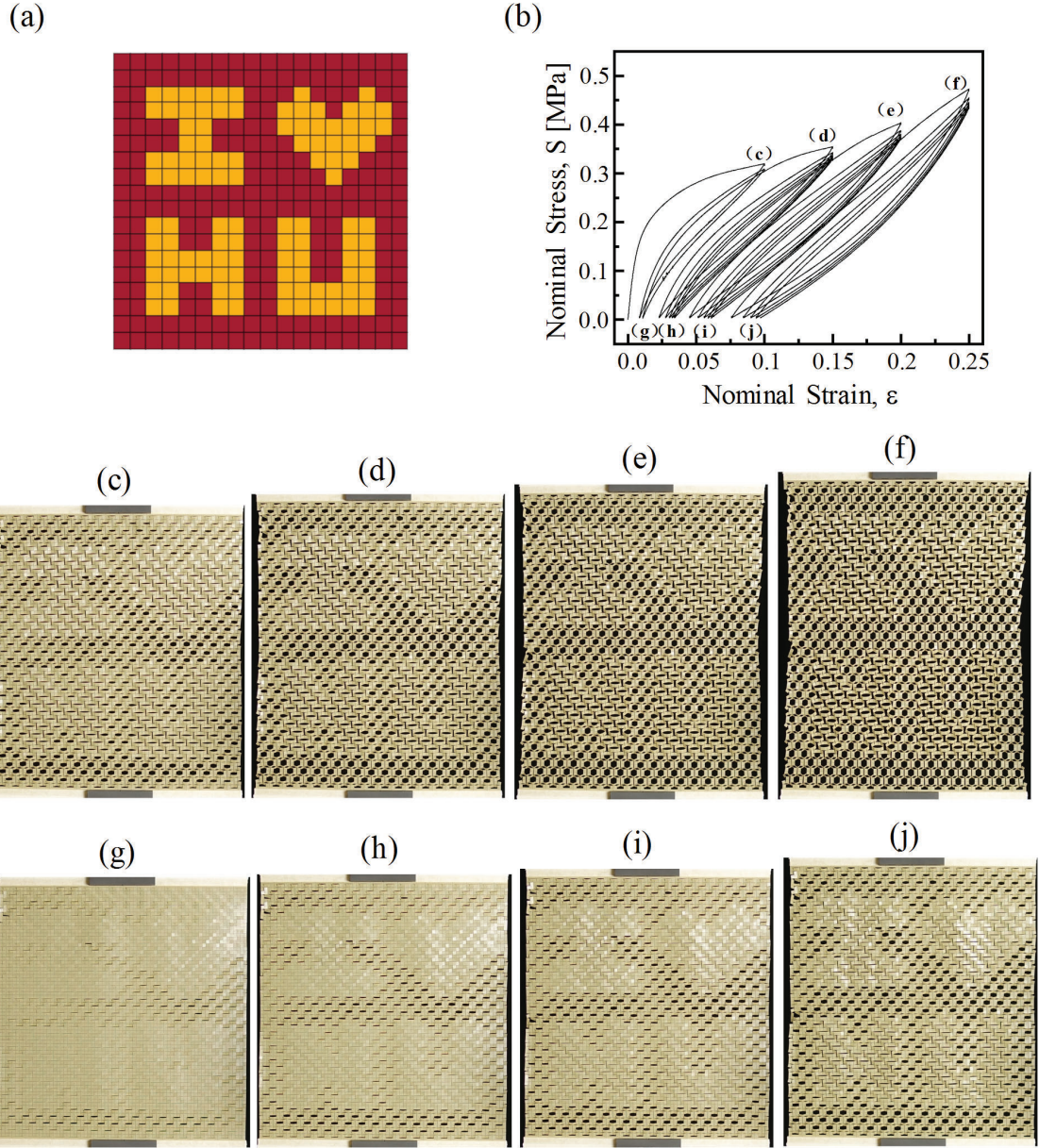


Figure S22: (a) Schematic of a kirigami textured surface with embedded "IHU". The yellow region is characterized by $\delta_1^{(1)}/l = 0.125$, $\delta_2^{(1)}/l = 0.0525$ and $\gamma^{(1)} = 0^\circ$ and the red region is characterized by $\delta_1^{(2)}/l = 0.15$, $\delta_2^{(2)}/l = 0.0525$ and $\gamma^{(2)} = 90^\circ$. (b) Stress-strain response recorded during a cyclic test. (c-j) Experimental images captured right after the applied strain is increased to $\epsilon = 0.1, 0.15, 0.2$ and 0.25 and then the load is dropped to zero.

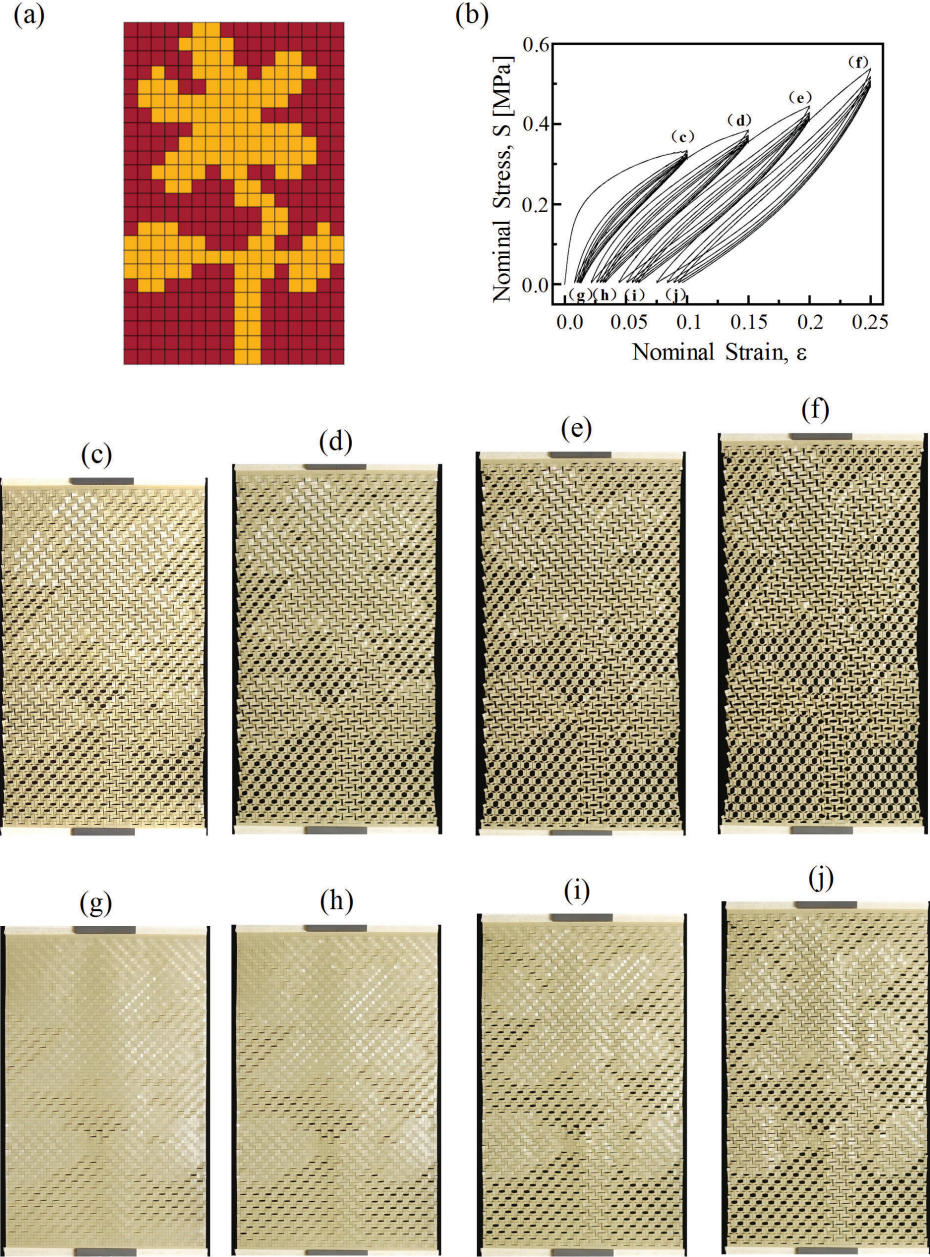


Figure S23: (a) Schematic of a kirigami textured surface with embedded a flower. The yellow region is characterized by $\delta_1^{(1)}/l = 0.125$, $\delta_2^{(1)}/l = 0.0525$ and $\gamma^{(1)} = 0^\circ$ and the red region is characterized by $\delta_1^{(2)}/l = 0.15$, $\delta_2^{(2)}/l = 0.0525$ and $\gamma^{(2)} = 90^\circ$. (b) Stress-strain response recorded during a cyclic test. (c-j) Experimental images captured right after the applied strain is increased to $\varepsilon = 0.1, 0.15, 0.2$ and 0.25 and then the load is dropped to zero.

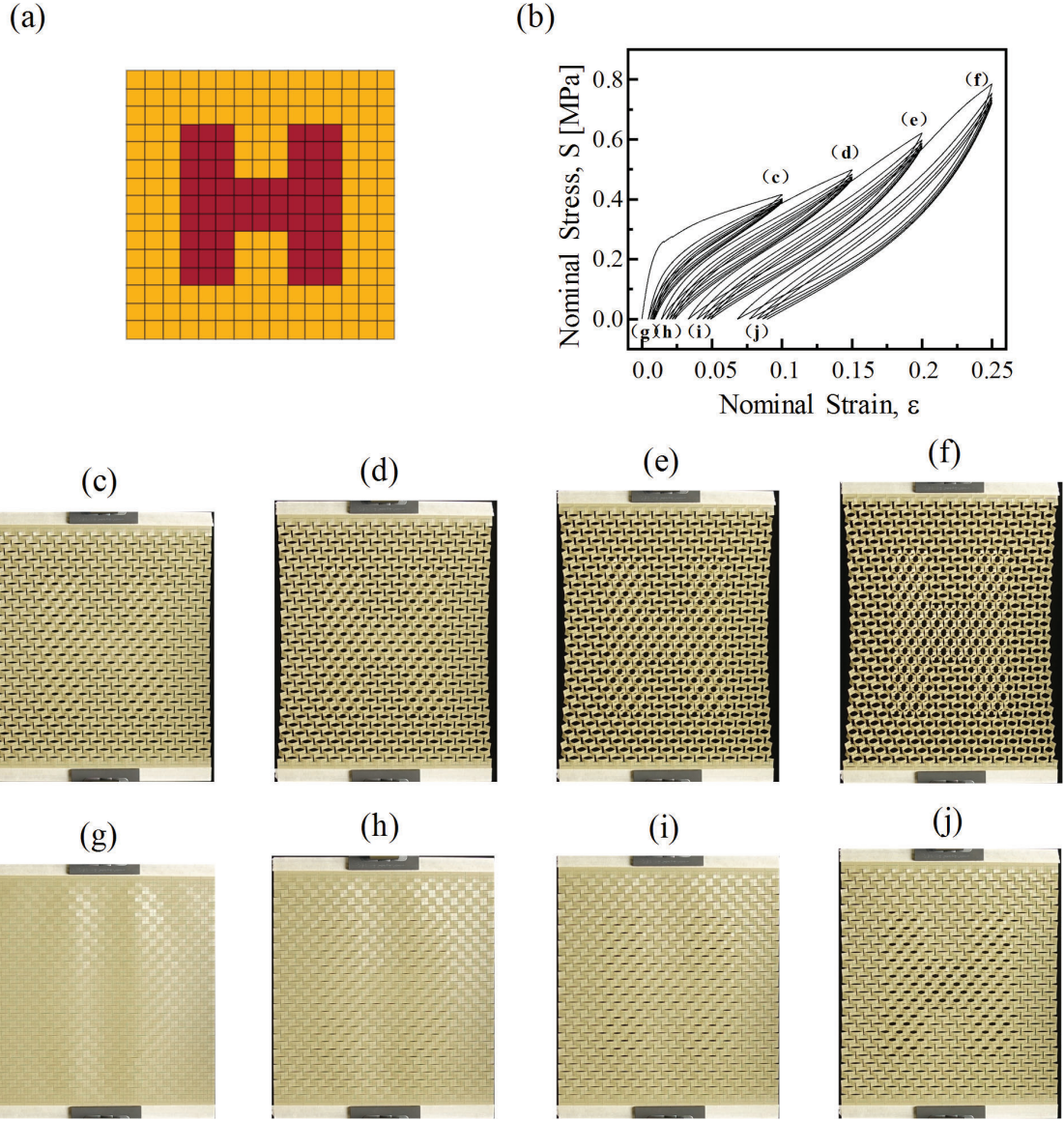


Figure S24: (a) Schematic of a kirigami textured surface with embedded an H. The yellow region is characterized by $\delta_1^{(1)}/l = 0.1375$, $\delta_2^{(1)}/l = 0.075$ and $\gamma^{(1)} = 0^\circ$ and the red region is characterized by $\delta_1^{(2)}/l = 0.15$, $\delta_2^{(2)}/l = 0.075$ and $\gamma^{(2)} = 90^\circ$. (b) Stress-strain response recorded during a cyclic test. (c-j) Experimental images captured right after the applied strain is increased to $\varepsilon = 0.1, 0.15, 0.2$ and 0.25 and then the load is dropped to zero.

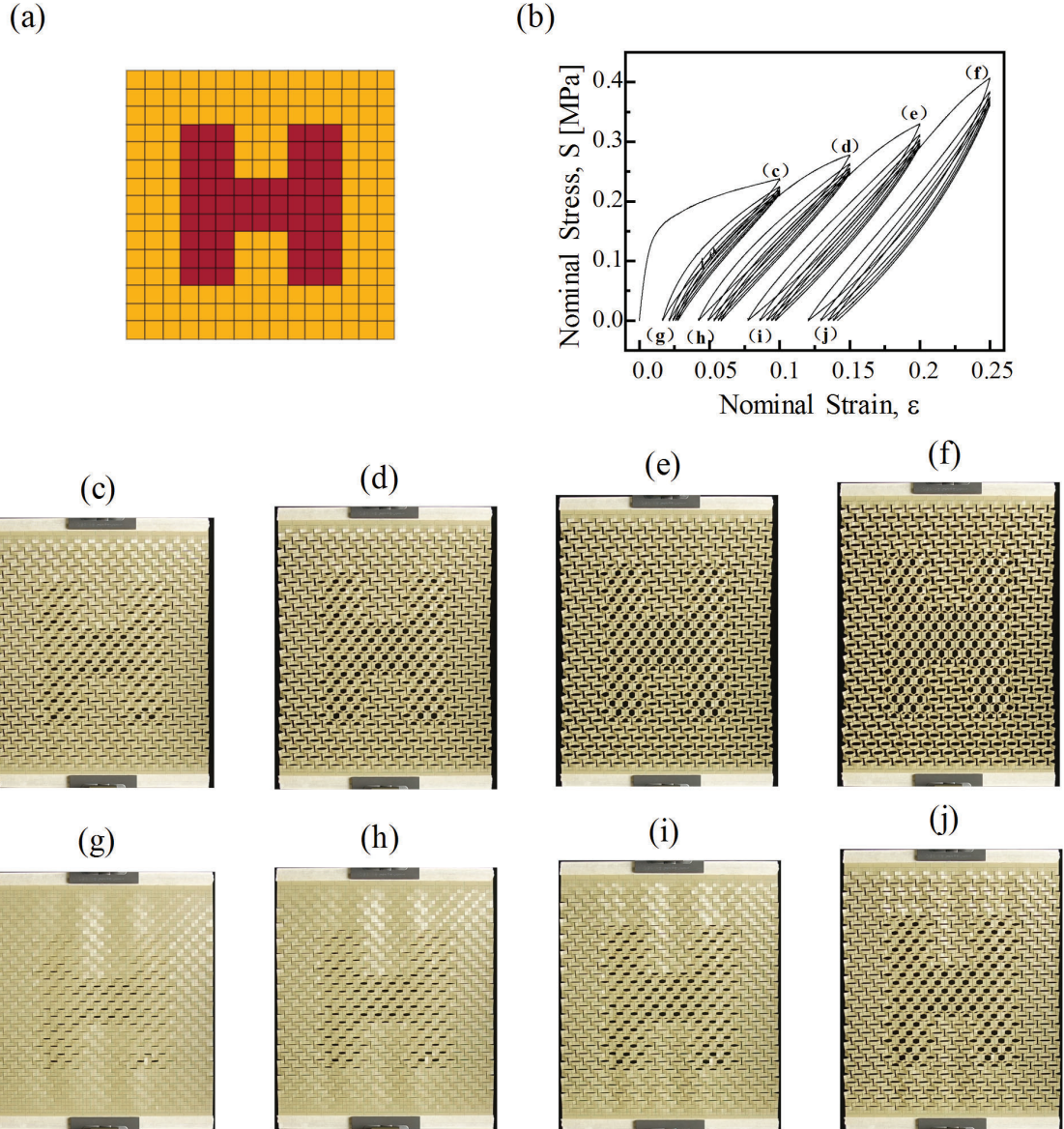


Figure S25: (a) Schematic of a kirigami textured surface with embedded an H. The yellow region is characterized by $\delta_1^{(1)}/l = 0.125$, $\delta_2^{(1)}/l = 0.0525$ and $\gamma^{(1)} = 0^\circ$ and the red region is characterized by $\delta_1^{(2)}/l = 0.15$, $\delta_2^{(2)}/l = 0.0525$ and $\gamma^{(2)} = 90^\circ$. (b) Stress-strain response recorded during a cyclic test. (c-j) Experimental images captured right after the applied strain is increased to $\epsilon = 0.1, 0.15, 0.2$ and 0.25 and then the load is dropped to zero.

IV. MOVIE CAPTIONS:

Movie 1 Uniaxial stretching of five individual samples.

Movie 2 Sequential behavior of *level 2* unit cells characterized by different δ_1/δ_2 values.

Movie 3 Sequential behavior of a heterogeneous surface comprising 2 build blocks.

Movie 4 Sequential behavior of a set of heterogeneous surfaces comprising 2 build blocks characterized by different length.

Movie 5 Sequential behavior of a heterogeneous surface comprising 3 build blocks.

Movie 6 Uniaxial stretching of kirigami textured surfaces.

References

- [1] A. Rafsanjani and K. Bertoldi. Buckling-induced kirigami. *Physical review letters*, 118(8):084301, 2017.
- [2] Andrew R Conn, Nicholas IM Gould, and Ph L Toint. *Trust region methods*, volume 1. Siam, 2000.
- [3] Jorge Nocedal and Stephen Wright. *Numerical optimization*. Springer Science & Business Media, 2006.